Unsteady force generation and vortex dynamics of pitching and plunging aerofoils

Yeon Sik Baik[1]†, Luis P. Bernal[1], Kenneth Granlund[2] and Michael V. Ol[2]

[1] Department of Aerospace Engineering, University of Michigan, Ann Arbor, MI 48105, USA

[2] Air Force Research Laboratory, Wright-Patterson Air Force Base, Dayton, OH 45433, USA

Experimental studies of the flow topology, leading-edge vortex dynamics and unsteady force produced by pitching and plunging flat-plate aerofoils in forward flight at Reynolds numbers in the range 5000–20 000 are described. We consider the effects of varying frequency and plunge amplitude for the same effective angle-of-attack time history. The effective angle-of-attack history is a sinusoidal oscillation in the range −6 to 22° with mean of 8° and amplitude of 14°. The reduced frequency is varied in the range 0.314–1.0 and the Strouhal number range is 0.10–0.48. Results show that for constant effective angle of attack, the flow evolution is independent of Strouhal number, and as the reduced frequency is increased the leading-edge vortex (LEV) separates later in phase during the downstroke. The LEV trajectory, circulation and area are reported. It is shown that the effective angle of attack and reduced frequency determine the flow evolution, and the Strouhal number is the main parameter determining the aerodynamic force acting on the aerofoil. At low Strouhal numbers, the lift coefficient is proportional to the effective angle of attack, indicating the validity of the quasi-steady approximation. Large values of force coefficients ($\sim$6) are measured at high Strouhal number. The measurement results are compared with linear potential flow theory and found to be in reasonable agreement. During the downstroke, when the LEV is present, better agreement is found when the wake effect is ignored for both the lift and drag coefficients.

Key words: low-Reynolds-number flows, swimming/flying, vortex dynamics

1. Introduction

The aerodynamics of pitching and plunging aerofoils captures unsteady flow phenomena relevant to several engineering problems of current interest. Of particular interest is the aerodynamics of flapping wings used by insects and small bird species for lift, propulsion and control. Flapping wings could provide superior manoeuvrability compared to fixed wings and rotary wings for small vehicles operating at low speeds (Maxworthy 1981; Platzer *et al.* 2008; Shyy *et al.* 2008). Flapping wings are commonly found in nature (Lighthill 1969), and have motivated researchers in fluid dynamics and biology to study the aerodynamics of birds and insects. An important unsteady flow feature found in bird and insect flight is the formation of vortical structures at the leading and trailing edges (Dickinson & Gotz 1993; Ellington *et al.* 1996). The formation of a leading-edge vortex (LEV) significantly enhances lift

† Email address for correspondence: yeon.baik@gmail.com

generation, which is crucial in sustaining flapping wing flight, but precise quantitative understanding of the increase in lift remains elusive.

A proposed explanation for increased lift generation by an attached LEV is the 'delayed stall' effect where the flow field remains attached beyond the steady stall incidence due to the presence of the LEV (Ellington *et al.* 1996). It has been suggested that the LEV is stabilized by spiralling axial flow within the vortex core; however, axial flow was not observed at very low Reynolds numbers, $Re = 120$ (Birch, Dickson & Dickinson 2004). Numerical studies by Shyy & Liu (2007) show that the stability and influence of LEV is likely to change as Re and other parameters associated with the flapping motion are varied. For transient motions, the impulsive acceleration of the model produces an LEV that generates high lift values beyond static stall, but a quick drop in lift is observed when the LEV separates after 2–4 chord lengths of travel (Dickinson & Gotz 1993; Jones & Babinsky 2010).

A different view on vortex formation and detachment was proposed by Gharib, Rambod & Shariff (1998) who studied the dynamics of vortex ring formation and noted that the vortex ring remains attached for small times until a relevant non-dimensional time, the 'formation number', reaches an optimum value of 4. In their view, the vortex ring separation process is a necessary topological change when the vortex is not able to accommodate any further increase in circulation (Dabiri 2009). A similar 'formation number' parameter was reported by Ringuette, Michelle & Gharib (2007) for low-aspect-ratio flat plates in transient motions. In this case the vortex forms at the edge of the plate and an increase in drag force due to the LEV was documented. Extensions of the formation number concept to other flow configurations have been reported by Milano & Gharib (2005) for a pitching–plunging plate in hover, and by Krueger, Dabiri & Gharib (2006) for a co-flowing jet. Dabiri (2009) reviewed the optimal formation number for biological propulsion. Rival, Prangemeier & Tropea (2009) investigated LEV formation in pitching and plunging aerofoils at reduced frequency $k = 0.25$ and concluded that LEV pinch-off occurs at formation times consistent with an optimal formation number as described by Dabiri (2009). However, as motion frequency increases, the time available for vortex development is reduced, and extension of these concepts to large reduced frequency is not obvious.

Formation of an LEV is also found in dynamic stall of helicopter blades (McCrosky 1981) and transient pitching motion of wings. McCrosky (1981) describes the dynamic stall vortex formed at the leading edge of an aerofoil due to sudden plunging and/or pitching motions. A temporary increase in lift coefficient well beyond the static stall of the aerofoil is recorded as the vortex convects in the chordwise direction. The dynamic stall vortex displays similar characteristics as the LEV, although most of the research on dynamic stall has been conducted at a much higher $Re = O(10^6)$ and lower reduced frequency than values found in flapping wing systems. The lift coefficient when the dynamic stall vortex is attached is in good agreement with classical steady aerodynamic theory, $c_l = 2\pi\alpha$, where α is the effective angle of attack (McCrosky 1982). After the dynamic stall vortex separates there is a significant reduction in lift coefficient. Dynamic stall vortices are also observed in rapid pitch-up manoeuvres of fixed wings which show very large force coefficients during the transient motion of the wing (Strickland & Graham 1987; Visbal & Shang 1989). The importance of LEV for lift generation is noted in all the aforementioned studies, but understanding the stability and development of LEV and its relation to wing kinematics is a major challenge in theoretical and approximate modelling of these flows.

Studies of the aerodynamics of flapping wings and pitching and plunging aerofoils in forward flight note the significance of reduced frequency and Strouhal number in the dynamics of the flow. The *St* range between 0.25 and 0.35 has been identified to produce high propulsive efficiency (Triantafyllou, Triantafyllou & Grosenbaugh 1992). A similar range of *St* was reported by Anderson *et al.* (1998) in harmonically pitching and plunging NACA0012 aerofoils, and this range also coincides with the *St* values found in numerous biological flyers (Taylor, Nudds & Thomas 2004). Strouhal number has been emphasized in numerous oscillating aerofoil flow visualization and wake measurement experiments (Koochesfahani 1989; Lai & Platzer 1999; Young & Lai 2004), where the wake structures that produce drag or thrust are dependent on the value of *St*. As suggested by Lighthill (1969), thrust-producing conditions are characterized by jet-like wakes where vortices are arranged to produce excess downstream momentum at the centre. Ohmi *et al.* (1990, 1991) found similar *St* dependence in wake structures for transient pitching of a NACA0012 aerofoil. More recently, experimental studies using particle image velocimetry (PIV) also emphasize the significance of *St* on the wake structure produced by pitching and plunging aerofoils at $Re = O(10^3)$–$O(10^4)$ (Lua *et al.* 2007; von Ellenrieder & Posthos 2008; Godoy-Diana, Aider & Wesfried 2009).

Another important parameter in forward flight of pitching and plunging aerofoils is the effective angle of attack, which is defined here as the angle formed by the aerofoil chord and the incoming stream for an observer moving with the aerofoil pivot point. Changes in *St* could be produced by changing the reduced frequency, k, or plunge motion amplitude, h_0. As noted by Read, Hover & Triantafyllou (2003), the relationship between *St* and effective angle of attack is nonlinear; changes in *St* also modify the effective angle-of-attack history. In order to isolate the effect of *St*, it is necessary to preserve the effective angle-of-attack history for all *St*. Read *et al.* (2003) recognized this problem and proposed that higher harmonics must be added to a sinusoidal plunge motion in order to preserve a sinusoidal effective angle-of-attack history. The study concluded that at high *St*, a sinusoidal effective angle of attack substantially increases the thrust coefficient compared to the effective angle of attack produced by a sinusoidal plunge motion. Hover, Haugsdal & Triantafyllou (2004) performed experiments with effective angle-of-attack histories consisting of a square wave, a symmetric sawtooth wave and a sinusoidal wave, and concluded that the sinusoidal wave produced the highest thrust efficiency. These studies suggest that preserving sinusoidal effective angle-of-attack profile at high *St* is a requirement to isolate the effect of *St*, and achieving high thrust and efficiency for pitching and plunging aerofoils in forward flight.

In the present research, we seek to elucidate the role of reduced frequency and Strouhal number on the aerodynamics of pitching and plunging aerofoils at low Reynolds numbers, $O(10^3)$–$O(10^4)$, for values of these parameters relevant to biological flight and the design of micro air vehicles. The current study isolates the effects of Strouhal number and reduced frequency on both aerodynamic force history and flow field evolution history. Since both pitch and plunge amplitude are free parameters (keeping the pitch pivot point fixed), pitch and plunge are combined through a definition of effective angle of attack. Namely, it is possible to retain one function of effective angle of attack against phase through relative changes in pitch and plunge amplitude, thus preserving *St*. Furthermore, several different *St* values are considered while retaining the aforementioned function of effective angle-of-attack history. We focus on a single effective angle-of-attack history with values large enough to result in formation of an LEV during each cycle. The dynamics and

stability of the LEV and its role in force generation as a function of Strouhal number and reduced frequency are also investigated. The unsteady force measurements from experimental results are compared with unsteady potential flow theory, which provides a useful theoretical framework for these flows. In addition, optimal formation number concepts at large reduced frequency are explored to gain a better understanding of the underlying vortex dynamics.

1.1. *Theoretical considerations*

Theoretical analyses of pitching and plunging aerofoils in forward flight were reported by Theodorsen (1935), Garrick (1936) and von Kármán & Sears (1938). These models were derived within the framework of linear potential flow theory, which implies inviscid fluid, small disturbances and a plane wake. It is also assumed that the flow at the trailing edge is smooth and there is suction at the leading edge. von Kármán & Sears (1938) noted that there are three contributions to the vorticity distribution and the unsteady lift: (i) the quasi-steady lift produced by the bound vorticity in the aerofoil; (ii) the apparent mass lift produced by the time rate of change of the bound vorticity; and (iii) the lift produced by the wake vorticity. Garrick (1936) studied the thrust produced by pitching and plunging aerofoils and noted that there are two contributions: (i) the leading-edge suction produced by the high-speed flow about the leading edge; and (ii) the projection in the flight direction of the pressure force on the aerofoil. In the present work, we consider aggressive pitch–plunge harmonic motions at high frequency and large amplitude with the same effective angle-of attack time history in all cases. These motions are well beyond the expected limit of applicability of linear theory. However, linear theory provides a very useful framework for the analysis of the experimental results. In the present work, harmonic effective angle-of-attack time history given by (1.1) is considered. Following von Kármán & Sears (1938), the unsteady lift time history can be expressed as the sum of contributions from effective angle-of-attack oscillations and pitch oscillations as shown by (1.2). Complex notation is used, with the real part being the physically relevant component:

$$\alpha_e(t) = \alpha_0 + \alpha_{e0}e^{i(2\pi ft - \phi)}, \tag{1.1}$$

$$c_l(t) = 2\pi\alpha_o + \frac{\pi c}{2U_\infty}\left(\frac{d\alpha_e}{dt} - \frac{c}{2U_\infty}\frac{d^2\theta}{dt^2}(2x_p - 1)\right) + 2\pi C(k)Q, \tag{1.2a}$$

$$Q = \alpha_e(t) - \alpha_0 + \frac{c}{2U_\infty}\frac{d\theta}{dt}(1.5 - 2x_p). \tag{1.2b}$$

Figure 1 illustrates the parameters used to describe pitching and plunging aerofoil kinematics. In (1.1) and (1.2), α_e is the effective angle-of-attack oscillation, with mean α_0 and amplitude α_{e0}, f is the frequency, t is time, ϕ is the phase lag between pitching and plunging motions, c is the chord of the aerofoil, U_∞ is the free stream velocity, θ is the prescribed pitching motion, and x_p is the pivot location measured from the leading edge and normalized by c. Additionally, k denotes the reduced frequency defined as $\pi fc/U_\infty$, and $C(k)$ is the Theodorsen function, which is complex-valued and depends only on k. The Q term is known as the circulatory term, where the value of $C(k)$ determines the effect of vorticity in the wake on the aerofoil vorticity distribution and lift. The value of $C(k)$ is equal to 1 for $k = 0$, which gives the quasi-steady limit where the contribution of the wake vorticity to the lift is not significant (von Kármán & Sears 1938; Bisplinghoff, Ashley & Halfman 1996, pp. 278–279). For the present experiments the values of α_0, α_{e0}, ϕ and x_p are the same for all cases, with $\phi = \pi/2$ and $x_p = 0.25$.
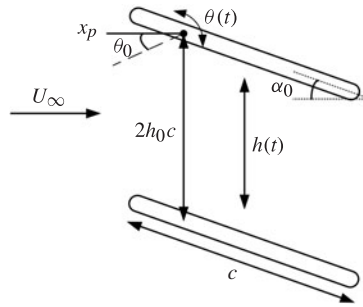
FIGURE 1. A schematic illustrating the parameters used to describe pitching and plunging aerofoil kinematics.

The effective angle of attack is given by (1.3) and has contributions from pitch and plunge motions. For harmonic $\alpha_e(t)$, the pitch motion is also harmonic and is given by (1.4). The plunge motion is not harmonic at large Strouhal number, $St = 2fh_0c/U_\infty$, and is given by (1.5). Thus

$$\alpha_e(t) = \alpha_0 + \theta(t) + \arctan\left(-\frac{1}{U_\infty}\frac{dh}{dt}\right), \tag{1.3}$$

$$\theta(t) = \theta_0 e^{i(2\pi ft - \phi)}, \tag{1.4}$$

$$h(t) = h_0 c F(t), \tag{1.5}$$

where $\theta(t)$ is the geometric pitch angle, θ_o is the pitch oscillation amplitude, and h_0 is the plunge motion amplitude normalized by the chord. The function $F(t)$ describes the plunge motion kinematics and is discussed in § 1.2. It is an even periodic function of the same period as the pitch oscillation. By construction, $F(0) = 1$ and $F(0.25/f) = 0$.

Substituting (1.1) and (1.4) in (1.2) gives the lift coefficient in terms of relevant non-dimensional parameters:

$$c_l(t) = 2\pi[\alpha_0 + \alpha_{e0}\sin(2\pi ft) + k\theta_0\cos(2\pi ft)],$$
$$+ \pi k\alpha_{e0}\cos(2\pi ft) - \frac{\pi}{2}k^2\theta_0\sin(2\pi ft)$$
$$+ 2\pi\,\mathrm{Re}\{(C(k) - 1)(\alpha_{e0}e^{i(2\pi ft - \pi/2)} + k\theta_0 e^{i(2\pi ft)})\}. \tag{1.6}$$

Equation (1.6) explicitly shows the three contributions to the lift on the aerofoil, namely: (i) quasi-steady lift (first term proportional to 2π); (ii) apparent mass (second and third terms); and (iii) wake (proportional to $C(k) - 1$). It is evident from (1.6) that k, h_0 and θ_0 are the parameters associated with unsteady lift generation in pitching and plunging aerofoils for given α_0 and α_{e0} values.

The drag coefficient is given by (1.7). The first term is the 'leading-edge suction' term, and the second term is the drag associated with the normal force component:

$$c_d(t) = -(\pi S^2 + \theta(t)c_l(t)), \tag{1.7a}$$

$$S = \frac{\sqrt{2}}{2}\,\mathrm{Re}\left\{2C(k)Q - \frac{c}{2U_\infty}\frac{d\theta}{dt}\right\}. \tag{1.7b}$$

The leading-edge suction, S, is derived by Garrick (1936) by computing the strength of the singularity at the leading edge. The leading-edge suction is in the axial direction. However, if an attached LEV forms, Polhamus (1966) argues that the leading-edge

suction should be normal to the aerofoil since the LEV acts as the leading edge of the aerofoil. The accuracy of the leading-edge suction on Garrick's formulation and the leading-edge suction analogy by Polhamus are examined in the current study.

1.2. *Plunge motion kinematics*

The effective angle-of-attack time history given by (1.3) can be written as (1.8) to result in a sinusoidal effective angle of attack. The nonlinearity from the arctangent function is replaced with a sinusoid as shown in (1.9):

$$\alpha_e = \alpha_0 + \theta_0 \sin(2\pi f t) + \alpha_{p0} \sin(2\pi f t), \tag{1.8}$$

$$\arctan\left(-\frac{1}{U_\infty}\frac{\mathrm{d}h}{\mathrm{d}t}\right) = \alpha_{p0}\sin(2\pi f t). \tag{1.9}$$

Here α_{p0} is the amplitude of the effective angle-of-attack oscillation produced by the plunge motion. The plunge motion is obtained by integrating (1.9) using the definition of $F(t)$ in (1.5). The limits of integration are chosen to satisfy the condition $F(0) = 1$, and the periodicity condition, $F(0.25/f) = 0$. The integral is shown in (1.10):

$$F(t) = 1 - \int_0^t \frac{U_\infty}{h_0 c}\tan(\alpha_{p0}\sin(2\pi f t'))\mathrm{d}t'. \tag{1.10}$$

The relationship between α_{p0} and Strouhal number can also be found from (1.10), and it is shown in (1.11):

$$St = \frac{1}{\pi}\int_0^{\pi/2}\tan(\alpha_{p0}\sin(\zeta))\,\mathrm{d}\zeta, \tag{1.11}$$

$$\theta_0 = \alpha_{e0} - \alpha_{p0}. \tag{1.12}$$

Finally, the pitch oscillation amplitude can be computed from (1.1) and (1.8), and it is shown in (1.12). The variations of α_{p0} and θ_0 with Strouhal number are shown in figure 2.

1.3. *Scope of the research*

The present research considers pitching and plunging flat plates with the same effective angle-of-attack history at varying frequency and amplitude of the pitch and plunge motions. The effective angle of attack is a sinusoidal oscillation from -6 to $22°$, with mean value $\alpha_0 = 8°$ and amplitude $\alpha_{e0} = 14°$. A pure plunging motion following this effective angle-of-attack history, as considered by Ol *et al.* (2009), is a deep stall condition where the maximum effective angle of attack is well beyond static stall. Ol *et al.* (2009) considered pitching and plunging SD7003 aerofoils at $Re = O(10^4)$ and $St = 0.08$, and they reported that the lift coefficient time history is in good agreement with linear theory predictions despite the presence of a large LEV. Rival *et al.* (2009) examined similar kinematics with the SD7003 aerofoil at $Re = 30\,000$ and k between 0.2 and 0.33. They examined the formation characteristic of LEVs during the dynamic stall process using PIV, and found that the LEV formation time is consistent with the findings of Gharib *et al.* (1998). The current study considers a larger St range up to 0.48 while preserving the same effective angle-of-attack profile and a Re range of 5000–20 000, with emphasis on the force time history and vortex dynamics.

The results are arranged in two groups of St: narrow range and wide range. The former features flow field velocimetry and vortex dynamics, while the latter emphasizes force measurement. The narrow range consists of six cases (N1–N6)
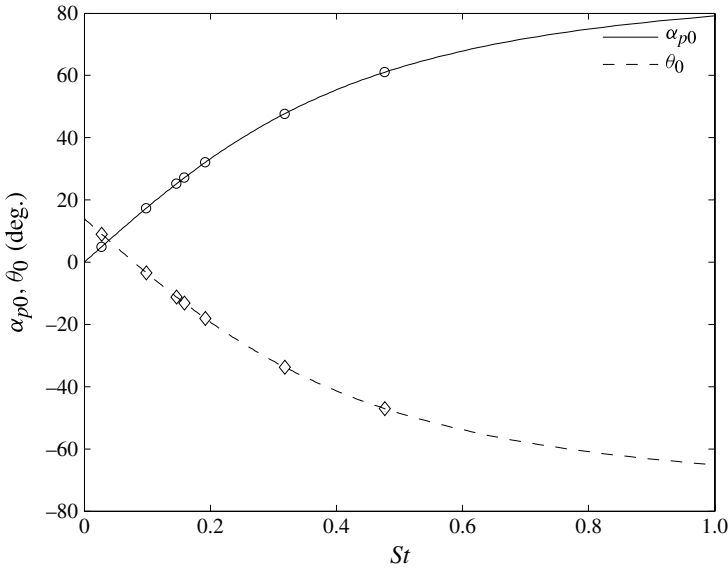
FIGURE 2. Maximum plunge effective angle-of-attack amplitude, α_{p0}, and pitch oscillation amplitude, θ_0, as functions of Strouhal number for the present study. The symbols show all the cases investigated in the present research, which are listed in table 1.

with St between 0.10 and 0.20. The Re based on the chord length of 152 mm is fixed at 10 000. Preliminary results for these conditions were reported by Baik *et al.* (2010). The wide range consists of five cases (W1–W5) with St of 0.16–0.48, motivated by the desire to address the St range found in most biological flyers (Taylor *et al.* 2004) with Reynolds number of 5000–20 000. Although flow field evolution and vortex dynamics data were also obtained for cases W1–W3, force measurements are the primary focus of the study. Figure 2 shows θ_0 as a function of St for the present studies, with specific values shown as open symbols. For the present conditions, the amplitude of the pitch oscillation is negative, which implies pitch down during the downstroke to reduce the effective angle of attack produced by the plunge motion. Parameters for the narrow and wide St range studies are listed in table 1.

The cases considered in the current study are shown in k–h_0 space in figure 3. Normalized plunge amplitude, h_0, is shown on the horizontal axis, and reduced frequency, k, on the vertical axis. Figure 3(*a*) illustrates the three different regimes considered in this research: constant h_0 (N1–N3), constant k (N3–N5) and constant St (N1, N5, N6 and N2, N4). The purpose of the three regimes is to discern the impact of k, h_0 and St on the flow development and topology. The wide St study considers higher values of St comparable to values reported for biological flyers. Similar flow regimes are considered to isolate the effect of relevant non-dimensional parameters in force generation.

2. Experimental set-up

Experiments were conducted in two water channel facilities: the University of Michigan water channel, and the Air Force Research Laboratory (AFRL) Horizontal Free-surface Water Tunnel.
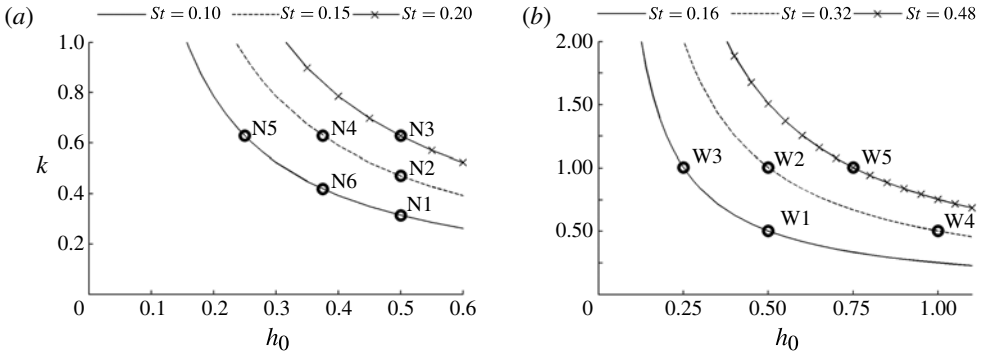
FIGURE 3. The k–h_0 space for (*a*) narrow *St* range study and (*b*) wide *St* range study.

Case	St	k	h_0	$|\theta_o|$ (deg.)	Period (s)
N1	0.10	0.314	0.500	3.39	22.70
N2	0.15	0.471	0.500	11.18	15.13
N3	0.20	0.628	0.500	18.09	11.35
N4	0.15	0.628	0.375	11.18	11.35
N5	0.10	0.628	0.250	3.39	11.35
N6	0.10	0.419	0.375	3.39	17.01
W1	0.16	0.500	0.500	13.16	7.13
W2	0.32	1.000	0.500	33.73	3.56
W3	0.16	1.000	0.250	13.16	3.56
W4	0.32	0.500	1.000	33.73	7.13
W5	0.48	1.000	0.750	47.06	3.56

TABLE 1. Case description of narrow *St* range (N1–N6) and wide *St* range (W1–W5) studies.

2.1. *University of Michigan water channel*

Particle image velocimetry (PIV) and force measurements were acquired in the low-turbulence water channel at the University of Michigan. A detailed description of the flow facility and instrumentation can be found in Baik (2011). Only a brief account highlighting the relevant features is presented here. The water channel facility has a test cross-section 61 cm wide by 61 cm high and the free stream velocity ranges from 6 to 40 cm s^{-1}. The measured turbulence intensity at free stream velocity of 6 cm s^{-1} is approximately 1 and 0.1 % for free stream velocity greater than 20 cm s^{-1}.

Photographs of the experimental set-up at the University of Michigan are shown in figure 4. Two flat-plate models of different chord were used: (i) chord length of 152 mm and $t/c = 0.023$ for the narrow *St* range study; and (ii) chord length of 76 mm and $t/c = 0.0625$ for the wide *St* range study. The models have rounded leading and trailing edges with radius equal to half the thickness. The flat-plate models were fabricated from stainless-steel plate and polished to minimize glare in the PIV images. The model spanned the depth of the water channel test section, and the distance between the model and the bottom of the test section was kept at approximately 1 mm. The cantilevered mounting scheme resulted in approximately $0.01c$ model tip deflection from hydrodynamic loading; however, the
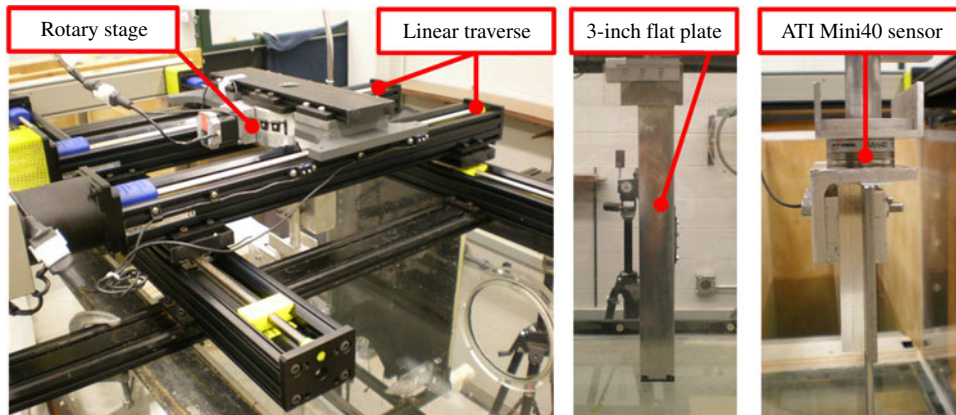
FIGURE 4. (Colour online) Experimental set-up at the University of Michigan water channel facility.

deflection at the half-span location where the PIV images were taken was found to be negligible.

The aerofoil motion was produced by a rotary stage (Velmex B4872TS/B4816TS rotary table) for the pitch motion, a linear traverse (Velmex 20-inch BiSlide) for the plunge motion, and the associated control system (Velmex VXM-1-1 motor controller). All the motors were stepper motors with accuracy of $\pm 0.0125°$ (B4872TS) and $0.05°$ (B4816TS) for the rotary stages, and ± 25 μm for the linear traverse. The aerofoil model can perform any arbitrary motion and was programmed to execute the motions described in § 1.3 within the stated position accuracy.

The PIV system includes a double-pulsed Nd:YAG laser (Spectra Physics PIV 300), light sheet forming optics, two dual-frame charge-coupled device (CCD) cameras (Cooke Corp. PCO.4000 equipped with a Nikon 105 mm Micro-Nikkor lens), a mechanical shutter, a signal generator, a delay generator, computer image acquisition system and custom-built control box. The PIV system and model motion apparatus were precisely synchronized using the custom-built control box to capture the desired phases of the motion. Phase-averaged PIV measurements are computed using 100-image ensemble averages. The PIV system period and the aerofoil motion period were matched with accuracy better than 0.1 ms, which resulted in a maximum relative displacement of the aerofoil between the first and last images of less than 5 pixels. The magnification used for the narrow St and wide St studies were 16 pixel mm^{-1} and 12 pixel mm^{-1}, respectively. The first five cycles of the motion were discarded in order to remove initial transient effects in the phase averages.

The water channel was seeded with 3 μm diameter titanium dioxide particles (Sigma-Aldrich) for the PIV measurements. A small amount (eight drops in the 5000 gallon water channel) of a dispersant (DARVAN C-N, Vanderbilt) was used to produce a uniform distribution of particles and to help maintain the particles in suspension. The incoming free stream velocity was aligned with the horizontal axis of the PIV images with an accuracy better than $0.1°$.

The PIV images were analysed using an in-house developed MATLAB-based PIV analysis software. The particle displacement was determined in two passes using cross-correlation analysis of displaced interrogation windows. The location of the cross-correlation peak was measured with subpixel resolution using a Gaussian fit of

the cross-correlation function around the peak. In the first, low-resolution pass, a fixed displacement equal to the free stream velocity and an interrogation window of 64 by 64 pixels were used; in the second, high-resolution pass, an interrogation window size of 32 by 32 pixels was used. Several validation criteria were applied to the measured particle displacements; the peak magnitude of the cross-correlation function must be at least three standard deviations above the mean, and the displacement must be within a predetermined range of values in the x and y directions. The PIV images were processed to obtain the velocity field on a square grid with 16 pixel spacing for all the images, which is consistent with the high-resolution interrogation window size and results in a spatial resolution of approximately 1 mm.

A median filter based on velocity vector values on spatially adjacent points was used to find the particle displacement at the points where the PIV validation failed. In addition, a 3σ filter was implemented to remove outliers associated with large sample-to-sample fluctuations. The 3σ filter was implemented in two steps. In the first step, the ensemble average and standard deviation are computed at all the points in the flow field. Then, each value was compared to ± 3 standard deviations of the mean value, and it was discarded if it was outside the 3σ range. The largest number of outliers was located in the high-shear region near the leading edge, and the maximum number of data points removed from the 3σ filter was approximately 10 % of the sample size.

Vorticity contours derived from PIV measurements are useful in visualizing the flow field but do not provide a robust algorithm for identifying the vortex core and its boundary. A popular method of identifying the vortex core and its boundary is to perform pointwise analysis of the velocity gradient tensor (Chakraborty, Balachandar & Adrian 2005). However, an important difficulty of this method is that it computes multiple maxima of the vortex core criterion within an enclosed high-vorticity region due to small-scale features of the vorticity field within the vortex. The vortex identification method proposed by Graftieaux, Michard & Grosjean (2001) overcomes this problem by introducing two scalar functions, Γ_1 and Γ_2, derived from the velocity vector fields, which identify the vortex core location and its boundary; the Γ_1 criterion identifies the vortex core, and the Γ_2 criterion identifies the boundary of a vortex. The Γ_1 and Γ_2 criteria are given by (2.1) and (2.2), respectively:

$$\Gamma_1(p) = \frac{1}{N} \sum_{i=1}^{N} \frac{((\boldsymbol{x_p} - \boldsymbol{x_i}) \times \boldsymbol{u_i}) \cdot \boldsymbol{n}}{\|\boldsymbol{x_p} - \boldsymbol{x_i}\| \cdot \|\boldsymbol{u_i}\|}, \tag{2.1}$$

$$\Gamma_2(p) = \frac{1}{N} \sum_{i=1}^{N} \frac{((\boldsymbol{x_p} - \boldsymbol{x_i}) \times (\boldsymbol{u_i} - \bar{\boldsymbol{u}}_p)) \cdot \boldsymbol{n}}{\|\boldsymbol{x_p} - \boldsymbol{x_i}\| \cdot \|\boldsymbol{u_i} - \bar{\boldsymbol{u}}_p\|}. \tag{2.2}$$

Here p is any point in the flow field, $\boldsymbol{x}$ is the position vector, $\boldsymbol{u}$ is the velocity vector, $\boldsymbol{n}$ is the unit vector in the z direction, N is the total number of points in a control volume, and $\bar{\boldsymbol{u}}_p$ is the average velocity evaluated using the same control volume. For the present study the values of Γ_1 and Γ_2 are computed at every point in the flow field using a 3×3 control volume (i.e. $N = 9$). The maximum values of Γ_1 and Γ_2 are 1 by construction. A vortex core typically has a $|\Gamma_1|$ value greater than 0.9, and a vortex boundary is characterized by $|\Gamma_2|$ values greater than $2/\pi$. A sample plot of the results of the vortex identification algorithm is shown in figure 5. Figure 5(a) shows contour plots of Γ_1 superposed on the velocity vector field. A vortex core is found at $x/c \approx 0.4$ since the other features in the contour plot do not reach a $|\Gamma_1|$ value of 0.9 required for a vortex core. Figure 5(b) shows the contour plots of $|\Gamma_2|$ also superposed
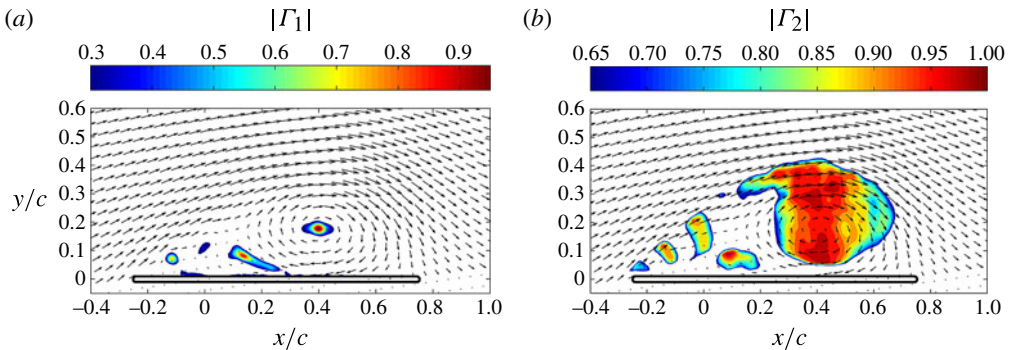
FIGURE 5. Vortex detection algorithm applied to a sample flow field with a leading edge vortex. (*a*) Vortex core location captured by $|\Gamma_1|$, and (*b*) its boundary given by $|\Gamma_2|$.

on the velocity vector field. The region where $|\Gamma_2|$ is greater than $2/\pi$ defines the vortex boundary associated with a vortex core. It is also noted that the $|\Gamma_2|$ criterion captures regions with rotational characteristics that may not have a vortex core. Once the vortex boundary is determined, the circulation can be computed by performing a summation of the z component vorticity enclosed by the vortex boundary. In what follows, a vortex location is defined as the coordinates of the maximum value of Γ_1 greater than 0.9. Furthermore, the area of the LEV is taken as the area interior to the contour $\Gamma_2 = 2/\pi$. This procedure was found to provide reliable and reproducible definitions of vortex core location and circulation.

The direct force measurement system consists of a force/torque sensor (ATI Industrial Automation Mini40 force/torque sensor), interface power supply (ATI Industrial Automation 9105-IFPS-1), a data acquisition card (National Instrument PCI-6625) and a computer. The attachment of the force/torque sensor to the aerofoil model is shown in figure 4. The Mini40 sensor is a six-component silicon strain gauge sensor capable of measuring forces in the plane of the aerofoil cross-section up to ± 80 N, and ± 240 N in the orthogonal direction. It also measures torque up to ± 4 N m in all three axes. The published resolution is $1/50$ N for force and $1/2000$ N m for torque. For these measurements the sensor axes are aligned with the aerofoil chord and chord-normal directions, which are converted to flow direction (drag) and lift direction using the known pitch angle, $\theta(t)$.

At each experimental condition, two different experiments were performed to obtain the force time history: a tare experiment and a force experiment. The tare experiments were performed in air to measure the inertial load on the force/torque sensor by lowering the water level without changing any other experimental parameter. The tare experiment results were subtracted from the force test results to obtain the hydrodynamic loading on the wing model. Similar to the PIV data acquisition, the force measurements were phase-averaged for each wing kinematic. A typical force measurement experiment consisted of 100 cycles with 5 s of pre-trigger data. The purpose of the pre-trigger data was to eliminate sensor bias. The first five and the last five cycles were discarded for two reasons. Firstly, discarding the first five cycles is consistent with the elimination of the initial transient effect used in PIV acquisition. Secondly, the force data were low-pass filtered using a zero-phase sharp frequency cutoff Fourier filter, which introduced significant initial and end transients lasting approximately three cycles. All the data sets were sampled at 2000 Hz and
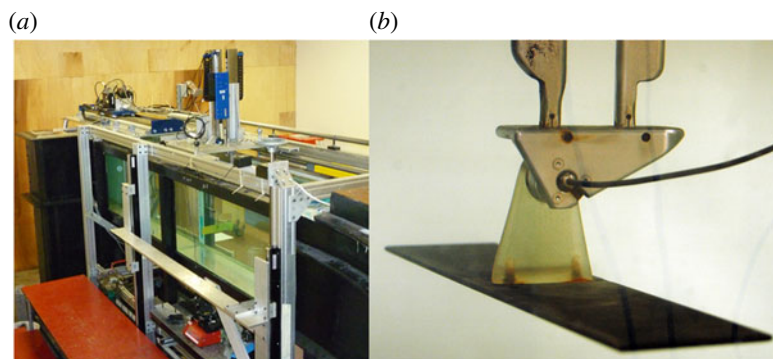
(*a*)   (*b*)

FIGURE 6. (Colour online) (*a*) Test section and portion of motion rig mounted above test section of the AFRL Horizontal Free-surface Water Tunnel. (*b*) Three-inch chord flat plate with force balance mounted between steel coupler piece and plastic foot connecting to the plate.

low-pass filtered with a cutoff frequency equivalent to approximately five times the motion frequency. The filter cutoff frequency was chosen to remove force sensor signal associated with structural resonance of the cantilevered wing, which was measured at approximately 6 Hz.

2.2. *Air Force Research Laboratory Horizontal Free-surface Water Tunnel*

The US Air Force Research Laboratory's Horizontal Free-surface Water Tunnel is fitted with a three-degree-of-freedom electric motion rig enabling independent control of pitch or rotation, plunge or heave, and 'surge' or streamwise-aligned translation. Photographs of the tunnel and the model installation are shown in figure 6. More detail on the rig operation is given in Ol *et al.* (2009) and Granlund, Ol & Bernal (2011), while the facility is discussed in Ol *et al.* (2005).

Force data are recorded from an ATI Nano-25 IP68 six-component integral sensor, oriented with its cylindrical axis normal to the pitch–plunge–surge plane. The sensor set-up is shown in figure 6(*b*). Sensor strain gauge electrical signals are analogue-to-digital converted in an ATI NetBox interface and recorded over an Ethernet LAN UDP protocol to a computer using a Java application. The time base of the ATI NetBox is inaccurate with the clock operating at a factor of 1.0023 faster than physical time. This is corrected in post-processing of data. A disadvantage of the IP68 waterproofing of the load cell is that it is sensitive to immersion depth in the cylindrical axis direction. Because this direction is normal to the plane of the motion of symmetrical models, the hydrostatic force will not affect normal force, axial force or pitching moment. Force and motion data are synchronized by polling for the trigger signal every 10 ms and starting the data recording when initial trigger is detected. All dynamic motions are repeated for 20 cycles, with the first three removed.

The force and moment signals are filtered in three steps. The first is a low-pass filter in the ATI NetBox at a frequency of 73 Hz to avoid introducing noise not correlated with motion force data, but without attenuating important fast non-circulatory 'load spikes'. The second step uses a moving average of 11 points to smooth the data while preserving as much of the non-circulatory load spikes as possible. This smoothing also makes a more numerically stable final step, which is a fourth-order Chebychev II low-pass filter with -20 dB attenuation of the stopband. The cutoff frequency is

five times the motion frequency. It is chosen for maximum passband flatness and high rejection of structural resonances, which may be just above the desired force frequency information range. To preclude time shift of useful data in the passband, the forward–backward filtering technique with the MATLAB '*filtfilt*' command is used.

Before each run, the load cell is zero-biased at model $\theta = 0°$, which is adjusted to horizontal with a bubble level. A static tare sweep over $-45° < \theta < 45°$ is performed with 500 samples of data every $2°$. Because the pitch angle is known throughout the motion, and the position error is negligible, the static axial force, normal force and pitching moment due to static model/sting/mount weight can be subtracted from the unsteady force data.

The dynamic inertial force and moment are only dependent on motion acceleration, in addition to the non-circulatory fluid loads. In order to remove all model inertial loads, the motions are also performed in air, from which the air static load is also removed. Finally, the forces in the model coordinate system are transformed to the tunnel free stream coordinate system of lift and drag and normalized by free stream dynamic pressure and planform area.

3. Results and discussion

3.1. *Flow topology and development*

Figure 7 shows superposed streamlines and normalized vorticity contours for the narrow *St* range cases derived from PIV measurements. At each flow condition, phase-averaged results are presented for phases in the range $t/T = 0.00$–0.75 with 0.083 (or $30°$) phase increment. For the narrow *St* study, the flow topology remains the same for all six cases; the formation of LEV is noted during the downstroke motion $(t/T = 0.00$–$0.50)$. The LEV is characterized by large negative vorticity bounded by a streamline terminating on the surface of the aerofoil. As the flow evolves in phase, the reattachment point of the bounding streamline moves downstream. A trailing-edge vortex (TEV) forms as the LEV separates and convects downstream. These topological features are expected and have been illustrated by Sane (2003) for example. The flow development, however, is not the same for all the cases; the vorticity contours suggest a strong correlation between the flow development and reduced frequency, *k*. Cases N3, N4 and N5, in the right-hand columns of figure 7, share the same value of $k = 0.628$, and the sizes and locations of the LEV with respect to the flat plate are in good agreement. Case N1, in the leftmost column of figure 7, with a lower value of $k = 0.314$, displays faster development compared to cases N3–N5. Similar observations can be made for cases N2 and N6 in comparison with higher *k*-value kinematics.

Figure 8 displays superposed streamlines and normalized vorticity contours for cases W1, W2 and W3 at selected phases of motion. Results are presented at phase increments $t/T \approx 0.083$ (or $30°$) for the entire period. The PIV image magnification is smaller compared to the narrow *St* cases to capture the near wake. The flow topology is very similar compared to the narrow *St* range study, but the flow development is slower due to higher *k* values. Cases W2 and W3 have $k = 1.0$ and the size of the LEV at the same phase is smaller than for case W1 and all the cases presented in figure 7. Case W2 has a pitch amplitude of $33.73°$, and it is interesting to note that the flow topology still remains the same despite the high rate of change of pitch angle. Owing to the large pitch angle, the wake is no longer planar, evinced by the LEV and TEV trajectories in the wake. The very similar flow development featured in cases W2 and W3 supports the conclusion that the *k* value governs the development rate of the LEV, as noted for the narrow *St* cases.
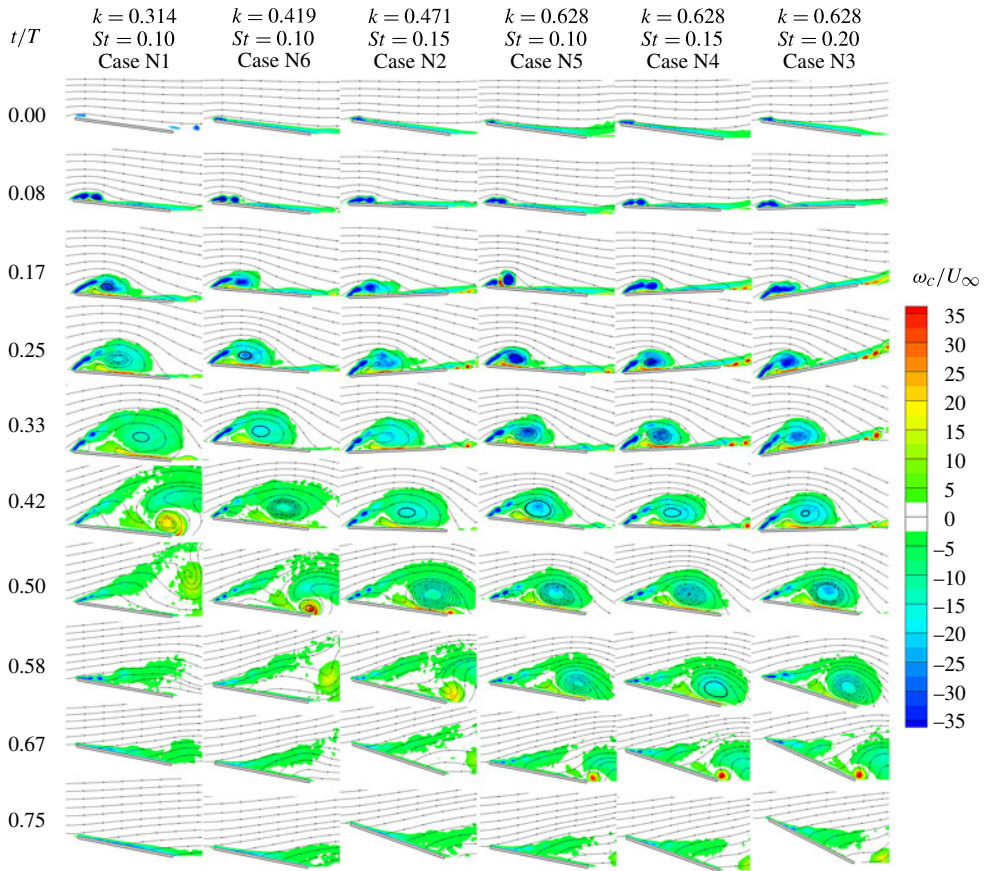
FIGURE 7. Normalized vorticity contours for narrow *St* range study.

The main observations from these experiments are: (i) a similar flow topology is found for all cases, which consists of the formation of an LEV and a closed recirculation region on the suction side of the aerofoil during each cycle; and (ii) the flow development rate is governed by the reduced frequency. The first observation highlights the importance of aerofoil geometry and effective angle-of-attack history since all cases have different k, St and h_0 values, but the same aerofoil shape and effective angle-of-attack history. Other aerofoil geometry or less aggressive effective angle-of-attack history may result in attached flow at the leading edge and a different flow topology during the motion, as shown by the results for an SD7003 aerofoil and for other kinematics reported by Ol *et al.* (2009), Rival *et al.* (2009) and Baik (2011). For the present case, vorticity in the separated shear layer at the leading edge advects into the LEV, forming a closed recirculation region. As the flow evolves in phase, the recirculation region and underlying LEV grows, resulting in downstream motion of the reattachment point until it moves past the trailing edge. At this point the recirculation region opens and the LEV vortex separates, which suggests a precise definition for LEV separation as the phase when the reattachment point reaches the trailing edge of the aerofoil. A TEV forms after LEV separation due to flow reversal at the trailing edge when the reattachment point moves past the trailing edge. Prior to LEV vortex detachment, the flow at the trailing edge is smooth and a thin wake
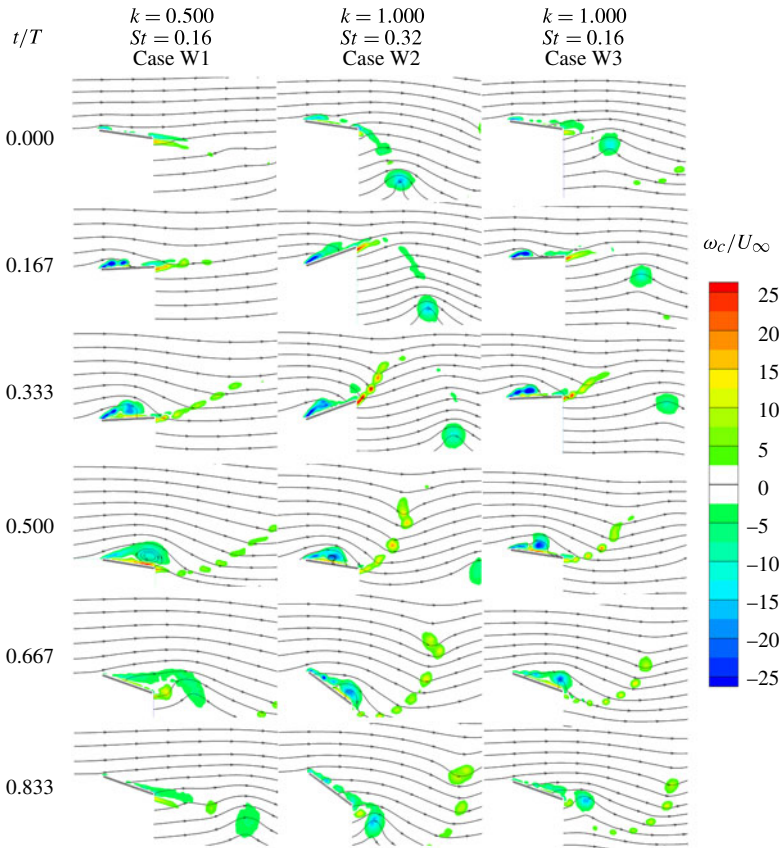
FIGURE 8. Normalized vorticity contours for wide *St* range study.

develops. A sequence of small vortices is observed, indicating vorticity being shed at the trailing edge and the onset of Kelvin–Helmholtz instability. The second observation suggests that the reduced frequency, k, controls the rate of flow development. At low k, the LEV has time to develop and separates before the end of the downstroke motion and a TEV forms during the downstroke. For $k = 0.628$ in the narrow *St* range cases or $k = 0.5$ in the wide *St* range cases, LEV separation occurs near the bottom of the downstroke, $t/T = 0.50$. At higher values of k, in the wide *St* range cases, a well-defined LEV is not observed until near the end of the downstroke. For $k > 0.471$, the LEV remains in close proximity of the aerofoil trailing edge in the initial phases of the upstroke that results in a strong interaction between the LEV and the aerofoil and delay in formation of the TEV. Clearly, there are two time scales at work in these flows: (i) the LEV development time scale, and (ii) the aerofoil motion time scale. The reduced frequency is the ratio of these two time scales. Only k values less than approximately 0.5 result in LEV detachment. These observations are further investigated in the next section, where the results on LEV dynamics are presented.

3.2. *LEV dynamics*

Analysis of the LEV strength, size and location for all cases was conducted using the vortex detection algorithm introduced in §2.1. Figure 9 presents the evolution of LEV circulation normalized by $U_\infty c$, and figure 11 shows the LEV area normalized by c^2.
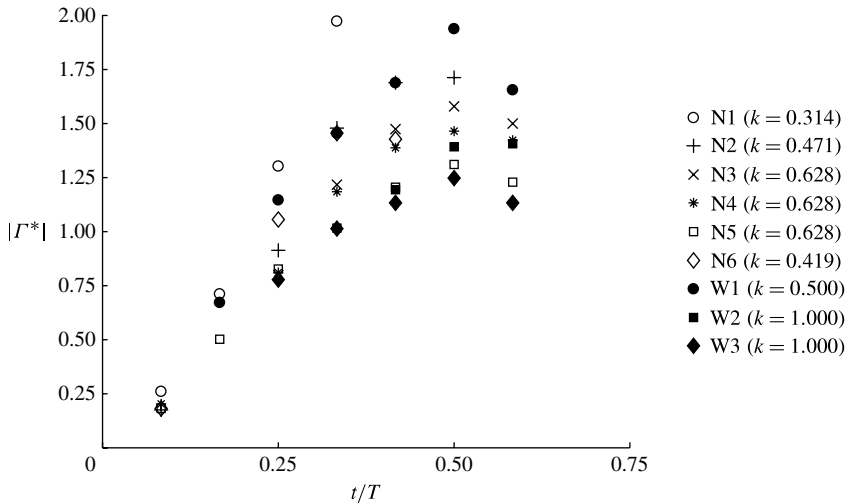
FIGURE 9. Normalized LEV circulation values as a function of t/T for all cases.

The LEV circulation and area are only reported when an LEV core is found; an LEV core exists when the maximum value of $|\Gamma_1|$ exceeds 0.9, and the core location is the location of the maximum (Graftieaux *et al.* 2001). There is good collapse of the data for the low-*St* range cases and high-*St* range cases, which were obtained with different chord lengths. Although the phase resolution is limited (30°), important trends are documented by the data.

The present data show that the circulation increases linearly with phase, and the growth rate depends primarily on reduced frequency, *k*, and to a lesser degree on Strouhal number, *St*. From the vorticity contours (see figures 7 and 8), it is evident that higher *k* kinematics show slower LEV growth rate. All the cases presented in figure 9 show a linear slope between t/T of 0.00 and 0.33. Case N1 with the lowest *k* value of 0.341 and $St = 0.1$ displays the fastest LEV circulation growth rate. The maximum normalized circulation is found at $t_{max}/T = 0.33$. At the next phase, $t/T = 0.42$, the data in figure 9 show that the LEV has detached and a TEV is formed. These results are in good agreement with the results reported by Rival *et al.* (2009) for an SD7003 aerofoil and the same effective angle-of-attack history but $k = 0.25$ and $St = 0.08$. Clearly, as *k* increases, the circulation growth rate decreases, which is a manifestation of the fact that, for the present measurements, the characteristic time for LEV formation is comparable to the motion period, as noted earlier. Another important feature is that, as *St* number increases, the LEV circulation also increases (cf. N3–N5 for $k = 0.625$ and $St = 0.2, 0.15$ and 0.1 respectively; or W2 and W3 for $k = 1$ and $St = 0.32$ and 0.16 respectively). The *St* number is the ratio of aerofoil motion speed to free stream speed, and an increase in *St* for fixed reduced frequency can be expected to produce an increase in circulation. However, these data show that the effect of *St* number on circulation is much less pronounced than the reduced frequency effect.

The results on LEV evolution in figure 9 also show that the LEV circulation reaches a maximum at a specific phase t_{max}/T. Figure 10 shows results for the phase and circulation at the maximum as a function of reduced frequency. Figure 10(*a*) shows the maximum circulation phase, t_{max}/T, as a function of *k* for all cases. The maximum
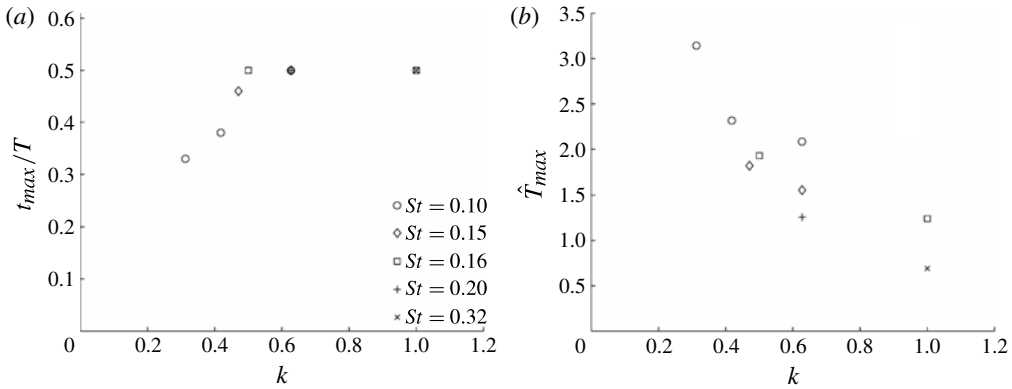
FIGURE 10. LEV vortex characteristics at maximum circulation. (*a*) Phase at maximum circulation; and (*b*) normalized LEV maximum circulation, as a function of reduced frequency.
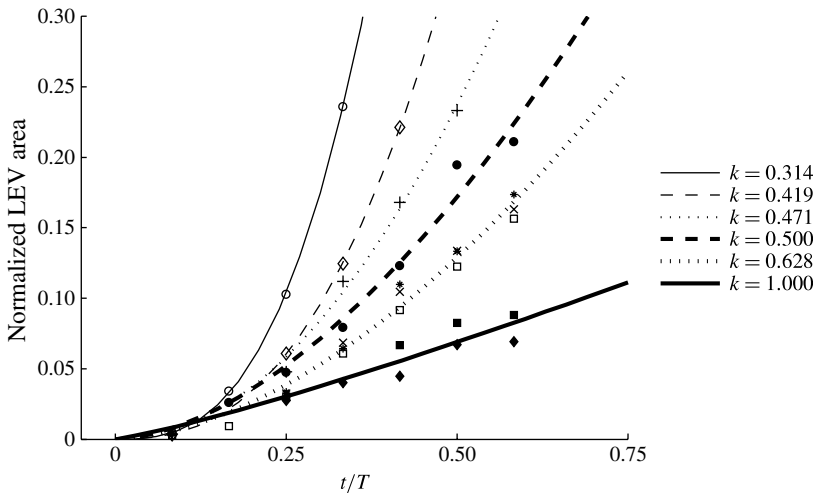

FIGURE 11. Normalized LEV area values as a function of t/T for all cases. Symbols are the same as shown in figure 9.

circulation phase increases linearly for $k < 0.5$, and it is constant at $t_{max}/T = 0.5$ for $k > 0.5$, which corresponds to the end of the downstroke. The reduction of circulation after the end of the downstroke is a kinematic effect, as the reversal of the motion results in a strong interaction of the LEV with the aerofoil and reduction of LEV circulation. In figure 10(*b*), the maximum LEV circulation normalized by the average leading-edge speed, the chord and a numerical factor as discussed by Rival *et al.* (2009) is plotted. This definition is consistent with the optimal formation number parameter introduced by Dabiri (2009) and it is shown in (3.1):

$$\hat{T}_{max} = \frac{\Gamma_{max}}{U_\infty c} \frac{1}{2\pi St}. \tag{3.1}$$

The results at low reduced frequency ($k = 0.314$, $\hat{T}_{max} \approx 3$) are consistent with the results of Rival *et al.* (2009) at the same point in the LEV evolution. The peak LEV circulation values are significantly less than the normalized maximum circulation value of approximately 4 found by Gharib *et al.* (1998) for vortex rings and the value 4.5 reported by Ringuette *et al.* (2007) for an unsteady flat plate normal to the incoming stream. In both of these cases, a vortex ring is allowed to form until it detaches. However, for the present cases, as the reduced frequency increases, the maximum LEV circulation decreases ($k = 1$, $\hat{T}_{max} \approx 1$).

In summary, the present results show several significant trends in the LEV vortex dynamics. Increases in reduced frequency result in significant reduction in the rate of LEV growth during the aerofoil motion cycle. At low reduced frequency $k < 0.3$, the aerofoil motion is slow enough for the quasi-steady vortex dynamics to dominate the LEV evolution. In this limit, the maximum LEV circulation is consistent with an optimal formation number parameter as discussed by Dabiri (2009) and Rival *et al.* (2009), although actual values of the non-dimensional circulation are somewhat lower than for other flows. As the reduced frequency increases, the LEV vortex dynamics is strongly influenced by the period of the oscillation, which limits the maximum circulation. Although reduced frequency is the main controlling parameter, it is also shown that increasing *St* increases the maximum LEV circulation, which is attributed to the increased motion speed associated with higher *St* number for fixed reduced frequency.

Figure 11 plots the normalized LEV area as a function of phase. A power-law curve fit was performed for the cases with the same *k* value and the results shown as lines in the figure. The equation for the power-law curve is: Normalized LEV area = $a\,(t/T)^b$, where *a* and *b* are real numbers. A correlation coefficient exceeding 0.9 was obtained for all cases, which supports the observation that *k* governs the formation characteristic of LEV. Contrary to the LEV circulation results, there is no maximum LEV area; an increase in LEV area is observed for all the cases as t/T is increased. These results are in agreement with results discussed in § 3.1 and point to the significance of reduced frequency in the topology and development of the flow. As reduced frequency is increased, the characteristic time of LEV development decreases compared to the period of the motion and the rate of change of LEV area decreases accordingly. These results also show that evolution of LEV area is independent of *St*.

The LEV core locations with respect to the flat-plate aerofoil for the narrow *St* range cases are plotted in figure 12(*a*). The trajectory is the same for all cases; however, the core locations occur at different phase for different kinematics. Also plotted in figure 12(*a*) is a second-order polynomial fitted to the core locations and the equation is given in the figure. The good collapse of the data suggest that the LEV trajectory is determined by the effective angle-of-attack history at low and moderate *St*. The LEV core locations for cases W1–W3 are plotted in figure 12(*b*). For comparison, cases from the narrow *St* range study (N2 and N4) are also plotted in the figure. The LEV core locations obtained for the wide *St* range study compare well with the LEV core trajectory for the narrow *St* range study, except for case W2 with $St = 0.32$, which is shown as a dotted line in figure 12(*b*). Case W2 has a pitch amplitude of 33.73° with motion period of 3.56 s, which introduces high pitch rates exceeding 100° s^{-1}, and it also has the lowest maximum circulation. At these conditions, the LEV forms farther away from the plate and moves closer, producing a stronger interaction with the aerofoil during the motion. Clearly for this case, pivot point location and effective angle-of-attack history will impact the LEV trajectory. In addition, *Re* has a small effect on the LEV trajectory, as shown by comparing
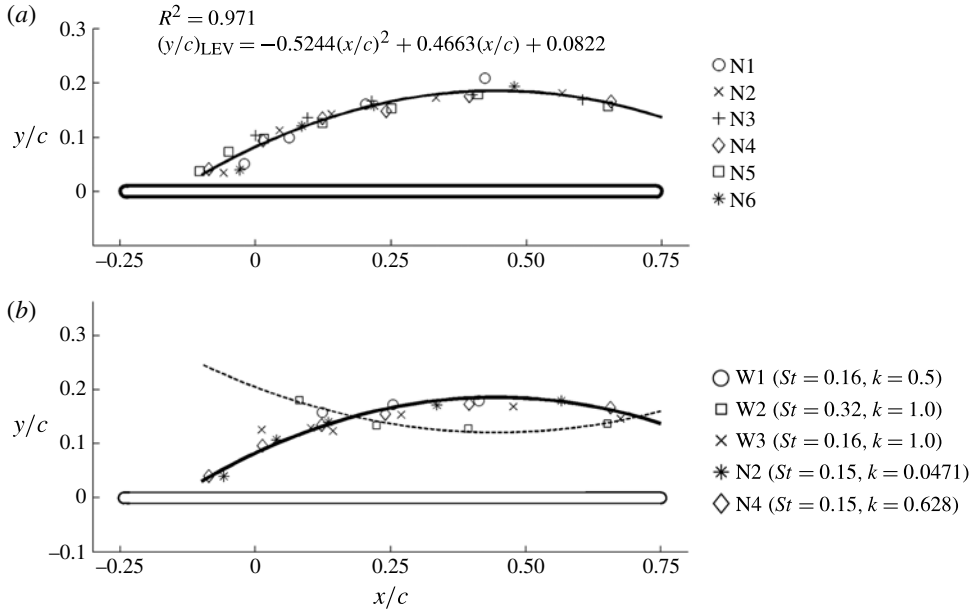
(*a*)

$R^2 = 0.971$

$(y/c)_{LEV} = -0.5244(x/c)^2 + 0.4663(x/c) + 0.0822$

○ N1
× N2
+ N3
◇ N4
□ N5
✳ N6

(*b*)

○ W1 ($St = 0.16$, $k = 0.5$)
□ W2 ($St = 0.32$, $k = 1.0$)
× W3 ($St = 0.16$, $k = 1.0$)
✳ N2 ($St = 0.15$, $k = 0.0471$)
◇ N4 ($St = 0.15$, $k = 0.628$)

x/c

FIGURE 12. LEV core locations for (*a*) narrow *St* range study and (*b*) wide *St* range study.

cases W1, W3 at $Re = 5000$, with cases N2, N4 at $Re = 10\,000$. These results show that the LEV vortex trajectory is independent of k, St and Re for a wide range of values of these parameters. Only the case with highest k and St shows a different trajectory. In this latter case, where there is a strong interaction of the LEV and the aerofoil, the pivot point location may also play an important role in the LEV evolution.

3.3. *Force measurements*

3.3.1. *Measurement uncertainty*

The measured phase-averaged axial, in the chord direction and plate-normal force time histories for $Re = 5000$, $10\,000$ and $20\,000$ are shown in figures 13–15, respectively. Also shown at selected phases are error bars of total length equal to twice the standard deviation of the sample. Measured force values in physical units are reported in order to document the measurement uncertainty for different facilities and experimental conditions. For the axial force, the uncertainty is strictly within 0.05 N for all cases, while the normal force shows an uncertainty less than 0.1 N. The measurement uncertainty is sufficient to resolve important features of the force time history as discussed below. Note the larger measurement uncertainty at the lower Re, and the smaller magnitude of the force in the axial direction compared to the normal direction. In these plots, a positive axial force is towards the trailing edge and normal force is in the positive lift direction.

Figures 13–15 show that the normal force increases with *St*. Cases W1 and W3 have the lowest *St* of 0.16, and case W5 has the highest *St* of 0.48. There is a monotonic increase in force with *St*, with smaller changes found for changes in reduced frequency. The force history has a maximum at $t/T \approx 0.25$ for all cases, and the minimum location shifts to later in the cycle as *St* increases. At $St = 0.16$, the minima are located at $t/T \approx 0.75$; while at $St = 0.48$, the minima are located
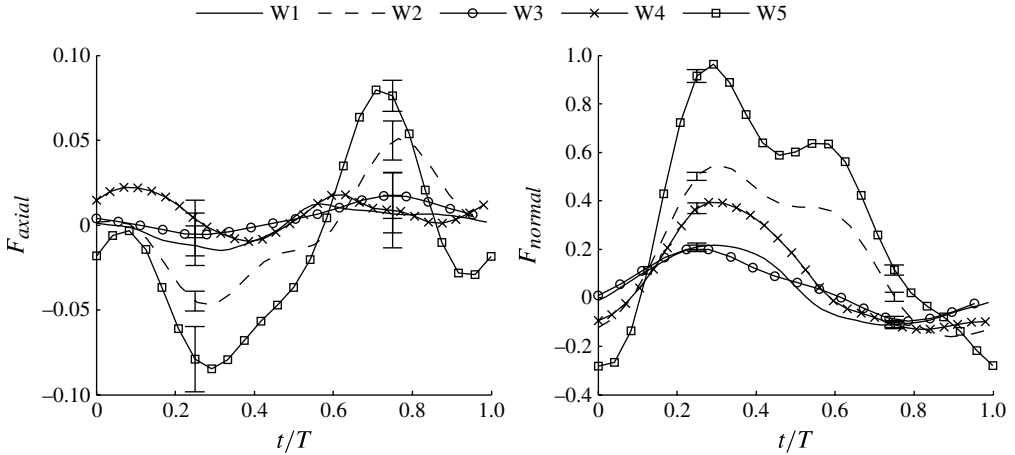
FIGURE 13. Axial and normal force profiles for $Re = 5000$ cases with measurement
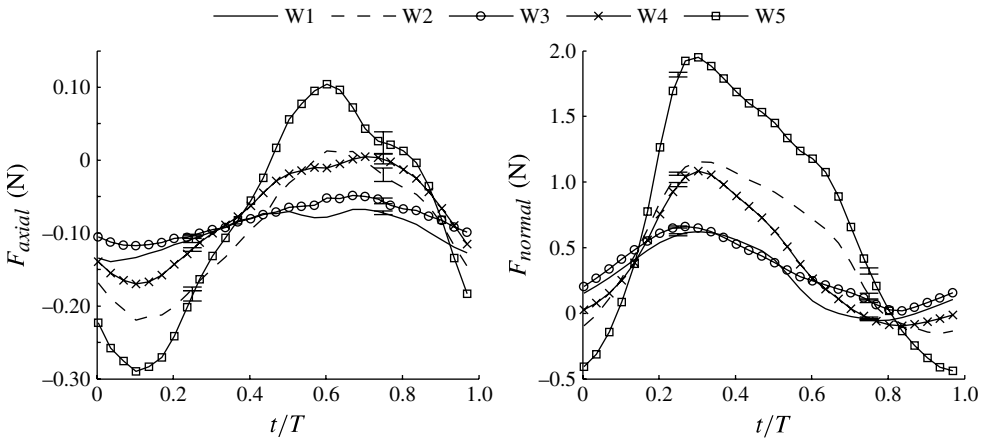uncertainties shown at $t/T = 0.25$ and 0.75.

FIGURE 14. Axial and normal force profiles for $Re = 10\,000$ cases with measurement
uncertainties shown at $t/T = 0.25$ and 0.75.

at $t/T \approx 1$. Furthermore, the force time histories are not symmetric about the maxima, showing larger normal force, and in some cases a second maximum, to the right of the main maximum, which is attributed to increased normal force produced by the LEV. The force time histories remain similar for all cases, which suggests small Re effects. However, for the present two-dimensional experiments, the increase in Re was achieved by increasing the free stream velocity, and therefore an increase in the force magnitude is expected. This makes direct comparison of normal force at different Re difficult. The effect of Re is discussed in the next section in terms of lift and drag coefficients.

The axial force results shown in figures 13–15 show relatively small axial force compared to the plate-normal force. The consistent change with St found for the normal force is not as well defined for the axial force. For $St = 0.16$, the measured
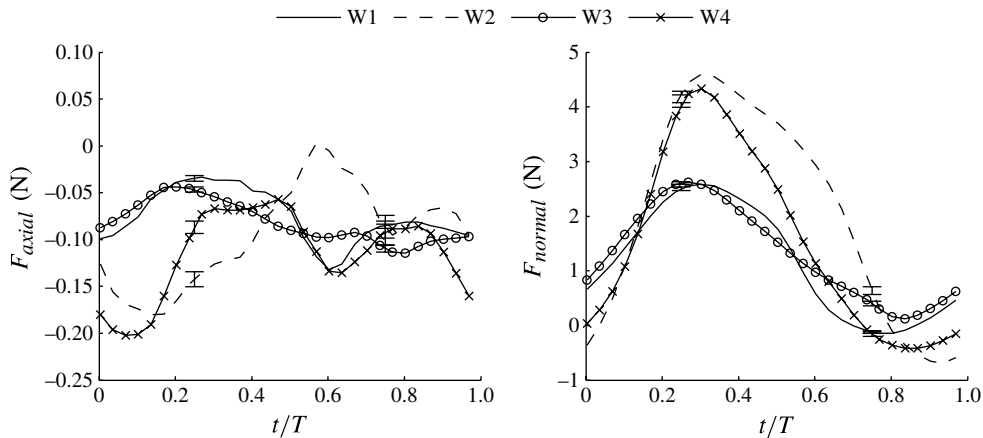
FIGURE 15. Axial and normal force profiles for $Re = 20\,000$ cases with measurement uncertainties shown at $t/T = 0.25$ and 0.75.

axial force is within measurement uncertainty for all cases. At higher St, the axial force increases and the axial force history changes with Re. At $Re = 5000$, the minimum (i.e. axial force towards the leading edge) is found at $t/T = 0.25$ and maximum at $t/T = 0.75$. In contrast, at $Re = 10\,000$, the minimum shifts to $t/T = 0.1$ and the maximum to $t/T = 0.6$. At the highest Re, the minimum is at $t/T = 0.1$ and there is no well-defined maximum. It should be noted that other effects like leading-edge curvature and plate thickness may also contribute to these changes. Although these effects in axial force history are not well understood, the force normal to the plate is an order of magnitude larger than the axial force, which is expected for the relatively thin plates used in this study and imply that friction and leading- and trailing-edge suction effects are small compared to the normal pressure force acting on the wing. It follows that, while there may be interesting features in the axial force histories, their contribution to the lift and drag profiles discussed in the following sections is relatively small.

3.3.2. *Case description and Reynolds number effect*

The lift coefficient histories for the wide St range cases are summarized in figure 16. The main observable trend in force coefficient histories is that they are primarily a function of St, with small changes produced by reduced frequency. This is in sharp contrast with the flow evolution results discussed previously, where it was found that reduced frequency was the main controlling parameter and St produced much smaller changes. Large lift coefficient values are recorded during the downstroke motion of the aerofoil as St is increased, with case W5 at $St = 0.48$ displaying a maximum lift coefficient of approximately 6. These force coefficient values are well beyond the prediction of steady aerodynamic theory of $2\pi\alpha_{eff}$, where α_{eff} is the effective angle of attack. In addition, the peaks are located at approximately $t/T = 0.25$, which corresponds to the middle of the downstroke motion where α_{eff} is maximum.

Figure 17 shows measured drag coefficients for the wide St range cases. Similar to the lift coefficients, the drag coefficients depend primarily on St. The maximum thrust and drag peaks are located at approximately $t/T = 0.25$ and $t/T = 0.75$, respectively. The maximum thrust coefficient exceeding 6 is recorded for case W5 ($St = 0.48$), which is comparable to the lift coefficient obtained at the same phase. In general, the
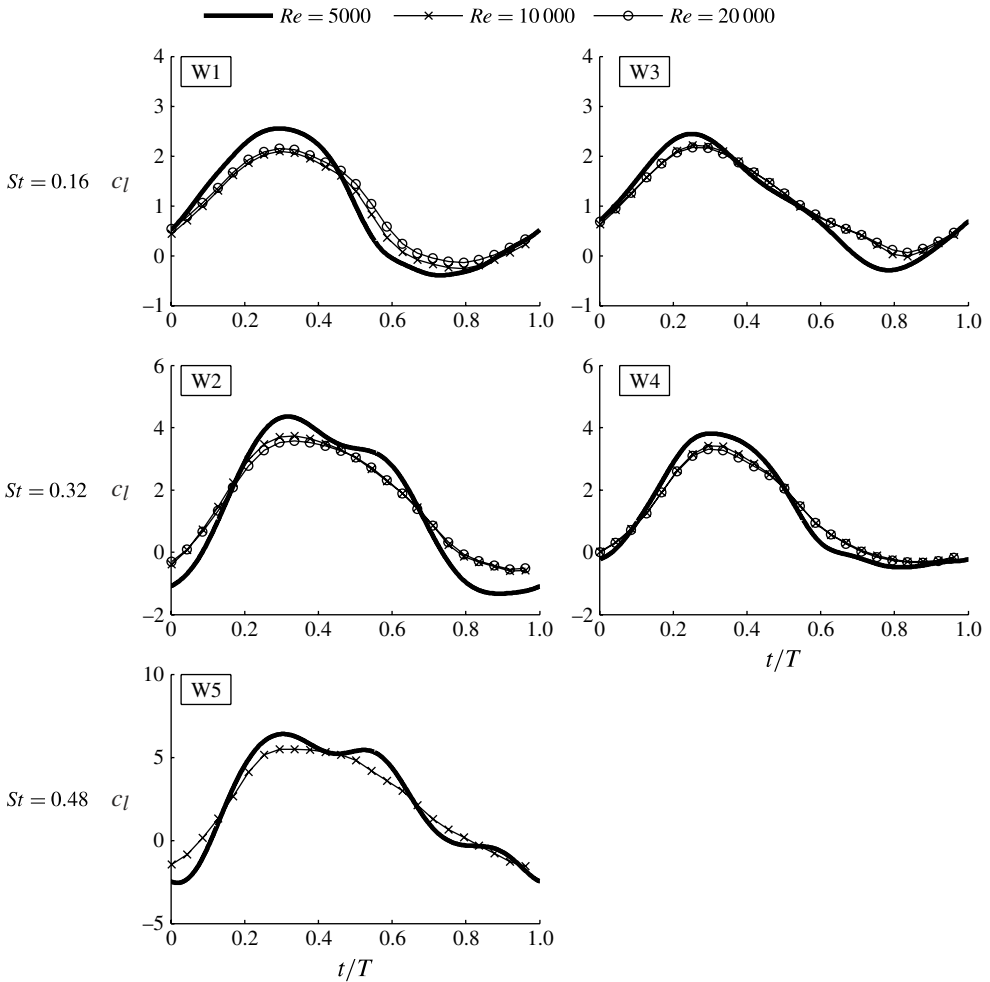
FIGURE 16. Lift coefficients for cases W1–W5 as a function of phase motion, t/T, for $Re = 5000$, $10\,000$ and $20\,000$.

current effective angle-of-attack profile produces thrust during the downstroke and drag during the upstroke.

Figures 16 and 17 show that the effect of Re on aerodynamic force is small. Qualitative features are the same for all Re for both lift and drag. There are small discrepancies in peak magnitudes, which can be accounted for by measurement uncertainty. In addition, the flat-plate thickness was 6.25 % for $Re = 5000$, and 2.3 % for $Re = 10\,000$ and $20\,000$. The difference in plate thickness may contribute to differences in LEV strength.

The time histories of the lift and drag coefficients for cases W1–W5 are shown in figure 18. Only $Re = 5000$ results are shown for clarity. Also plotted in figure 18 is the potential flow solution for steady flow. Ol *et al.* (2009) showed that for an SD7003 aerofoil at $St = 0.08$ and $Re = 60\,000$ the steady flow solution provides a good estimate of the lift coefficient history during the cycle. Computations of the lift coefficient for SD7003 and flat plates at $Re = 60\,000$ for the present effective
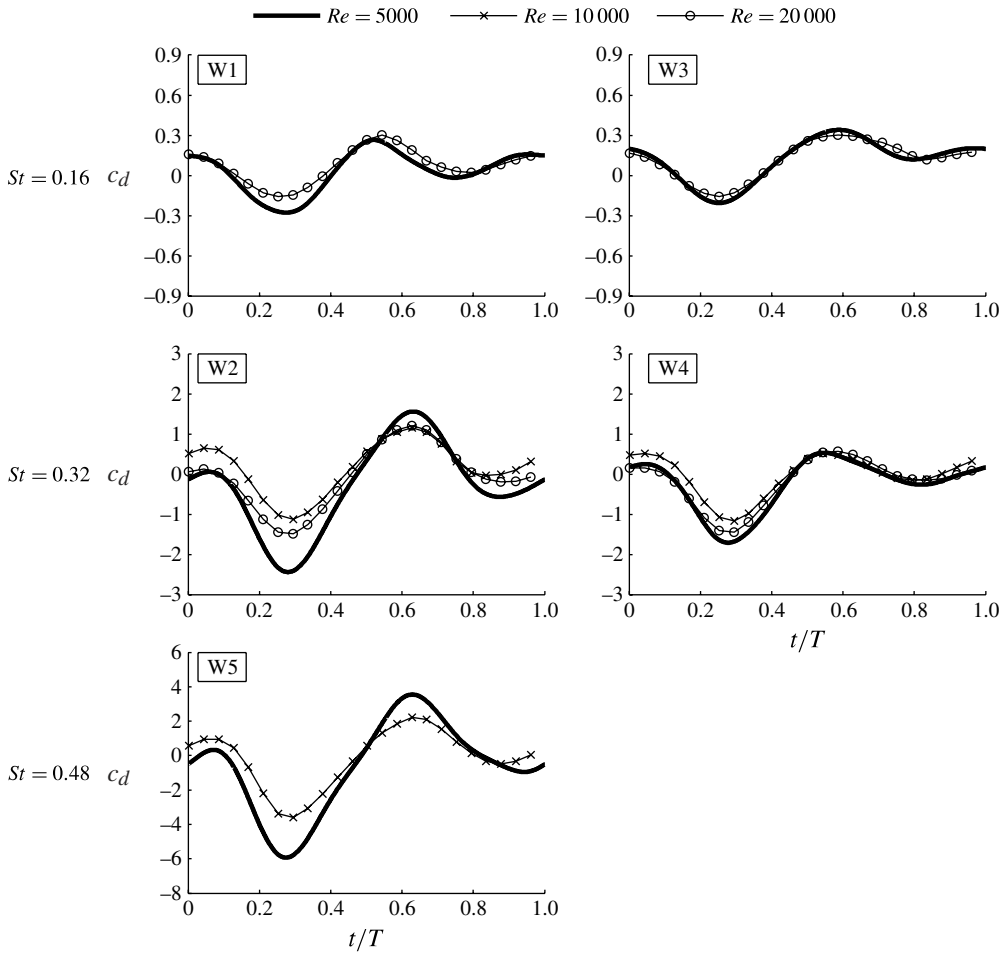
FIGURE 17. Drag coefficients for cases W1–W5 as a function of phase motion, t/T, for $Re = 5000, 10\,000$ and $20\,000$.

angle-of-attack history by Kang *et al.* (2009) also support this observation. The present data for $St = 0.16$ are in good agreement with the $2\pi\alpha_{eff}$ curve, which further supports the observations of Ol *et al.* (2009). A closer look shows that the lift coefficient for $0.25 < t/T < 0.5$ is slightly above the $2\pi\alpha_{eff}$ curve. This feature changes with reduced frequency: at high reduced frequency, the slower development of the LEV delays the increase in lift coefficient to later in the cycle. As St increases, the curve deviates from the quasi-steady value of lift coefficient but the lift peak remains at $t/T \approx 0.25$ for all cases. However, at $t/T \approx 0.75$, all the cases share a similar value of $c_l \approx -0.5$ despite the changes in St. For the drag coefficient, it is clear that increasing St increases the peak thrust. At $t/T \approx 0.50$, all the cases show a transition from thrust to drag, with higher St kinematic producing higher drag peak during the upstroke motion.

While St clearly emerges as the main controlling parameter for force coefficient time history of pitching and plunging aerofoils, the effect of reduced frequency is apparent by comparing cases W1 and W3, and cases W2 and W4. During the upstroke motion, cases W3 and W2 show higher lift coefficients than cases W1 and W4,
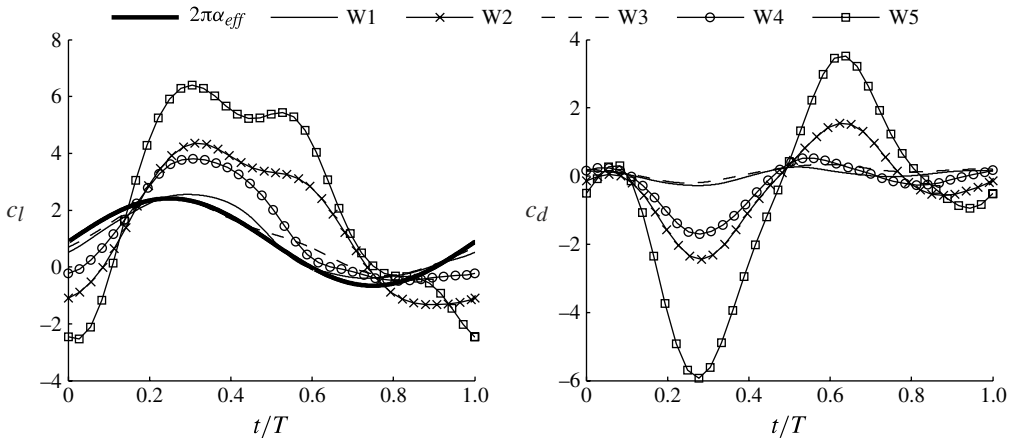
FIGURE 18. Lift and drag coefficients for cases W1–W5 as a function of t/T for $Re = 5000$.

respectively. In §3.1, it was found that an increase in k delays the formation of LEV, and it follows that kinematics with higher k will retain more lift at later phases of the motion, since the delay will result in delayed LEV convection.

Despite the discrepancy in the measured peak force coefficients at different Re, the presented data establish the link between St and peak force coefficients, with smaller effects caused by reduced frequency. In addition, it will be shown in §3.3.3 that the mean force coefficient values are in good agreement for all Re.

3.3.3. *Comparison with theory*

The success of linear potential flow theory in providing a reasonably accurate estimate of the lift coefficient history at low St suggests that unsteady potential flow theory may also give reasonable estimates at higher St. More recently, McGowan *et al.* (2011) have investigated the limits of applicability of linear theory for a pitching and plunging SD7003 aerofoil and found that it provides a good estimate of unsteady force coefficients at low St numbers. In this spirit, figure 19 compares the measured lift coefficient with unsteady potential flow theory (Theodorsen 1935), and with the Theodorsen model with $C(k)$ equal to 1, the quasi-steady limit, which corresponds to ignoring the effect of vorticity in the wake but retaining the quasi-steady and the apparent mass contributions to the lift. The theoretical results successfully capture the effects of St on lift. It is interesting to note that, for large effective angle of attack during the downstroke, Theodorsen's model with $C(k) = 1$ gives better agreement than the standard model. However, at small effective angle of attack during the upstroke, the standard model is more accurate except for case W5. Case W5 is the high-k and high-St case, which introduces a combination of delay in the LEV formation and significant pitch rates; a similar observation is made for case W2, which shares the same k as case W5 but at lower St value. Nonetheless, the good agreement with the Theodorsen model with $C(k) = 1$ suggests that the downstroke motion generates lift force without a contribution from vorticity in the wake. The vorticity contour plots in figure 8 show that formation of the TEV is delayed until after the LEV detaches or after motion reversal at the end of the downstroke. As a result, the increase in circulation from LEV temporarily increases the bound vorticity, which enhances lift generation. During the upstroke motion, the LEV convects downstream and detaches at the trailing edge of the aerofoil, followed by a subsequent shedding of a TEV. The
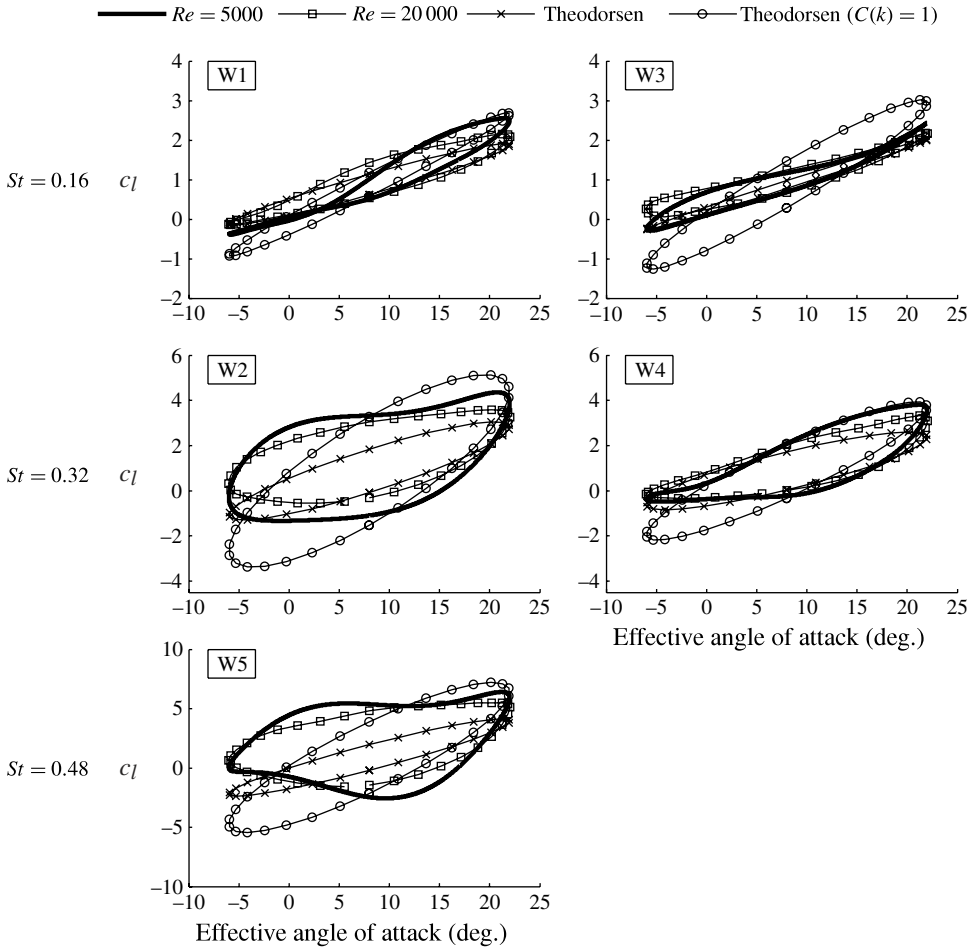
FIGURE 19. Measured lift coefficients compared with the standard Theodorsen model, and the Theodorsen model with $C(k) = 1$. For case W5 $Re = 10\,000$ is plotted instead of $Re = 20\,000$.

shedding of a TEV restores agreement with the standard Theodorsen model during the upstroke motion, although this does not exactly hold for cases W2 and W5.

Figure 20 compares the drag coefficient of individual cases with a modified Garrick model, and a modified Garrick model with $C(k)$ set to 1. The modified Garrick model presented in the figure excludes the leading-edge suction term and only accounts for the normal force component of the drag. The current study finds that the leading-edge suction term in Garrick's formulation significantly over-predicts the thrust generation during the downstroke. Similar to the lift coefficient, there exists a strong St dependence on the overall behaviour of the drag coefficients. The measured drag coefficients and the Garrick model with $C(k) = 1$ are in a good agreement during the downstroke motion. During the upstroke motion, the standard Garrick model compares better with the measured drag coefficient, especially for cases W1 and W4, which have lower k value compared to other cases. Cases W3–W5 show a lack of agreement with both models during the upstroke due to delayed shedding of LEV and TEV; the shed vortex significantly increases the pressure drag, which is not accounted for in Garrick's
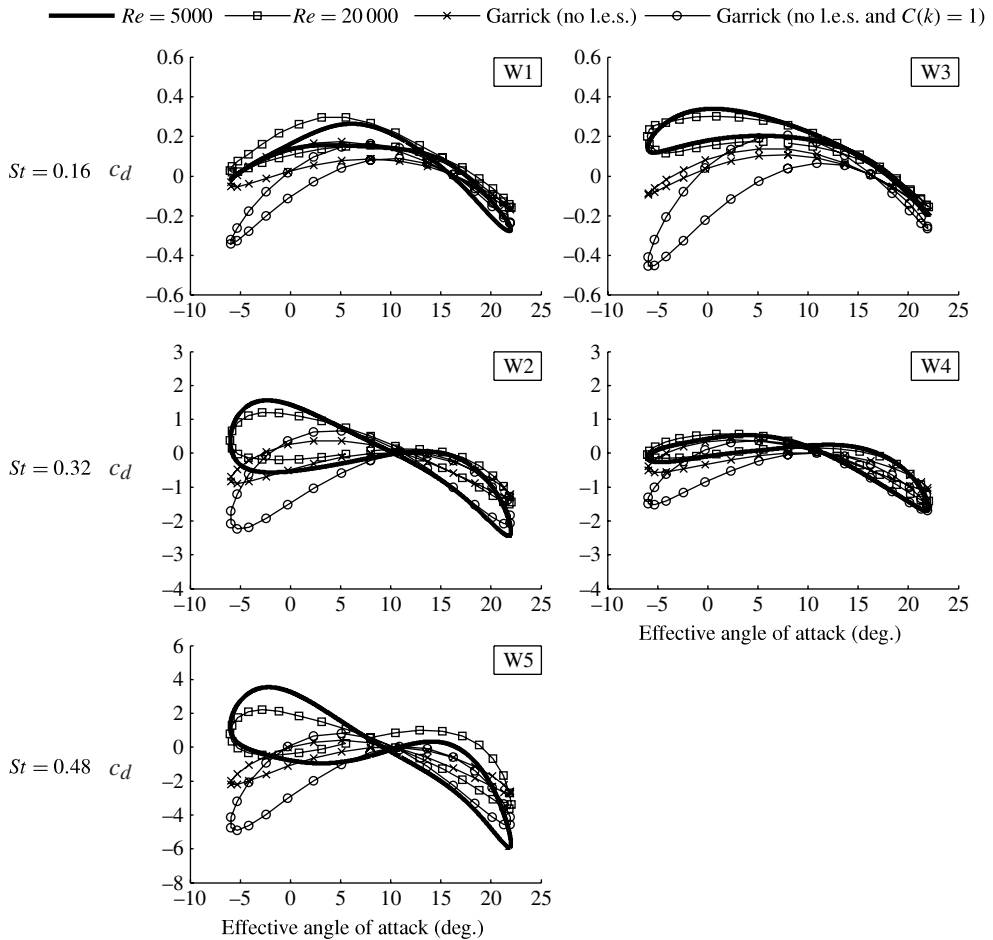
FIGURE 20. Measured drag coefficients compared with the Garrick model, and the Garrick model with $C(k) = 1$. The Garrick model only includes the drag force from the normal force component, exluding the leading-edge suction (l.e.s.) term. For case W5 $Re = 10\,000$ is plotted instead of $Re = 20\,000$.

formulation. Garrick's formulation shows thrust generation during the upstroke motion, and the magnitude is greater than during the downstroke because the magnitude of the geometric angle of attack is greater during the upstroke motion due to the positive 8° offset.

To examine the relevance of the leading-edge suction analogy (Polhamus 1966), figure 21 shows the combined result of the lift coefficient from the Theodorsen model with the leading-edge suction term from the Garrick model. In figure 20, it was shown that the Garrick model without the leading-edge suction term resulted in good agreement with the measured drag coefficient. It is assumed here that the leading-edge suction term contributes entirely to the lift, which is the basic assumption of the leading-edge suction analogy of Polhamus (1966) discussed in § 1.1. In order to test this analogy, the leading-edge suction term, πS^2, was directly added to the lift coefficient obtained from the standard Theodorsen model. The addition of the leading-edge suction term only affected the lift coefficients for the downstroke motion, as the
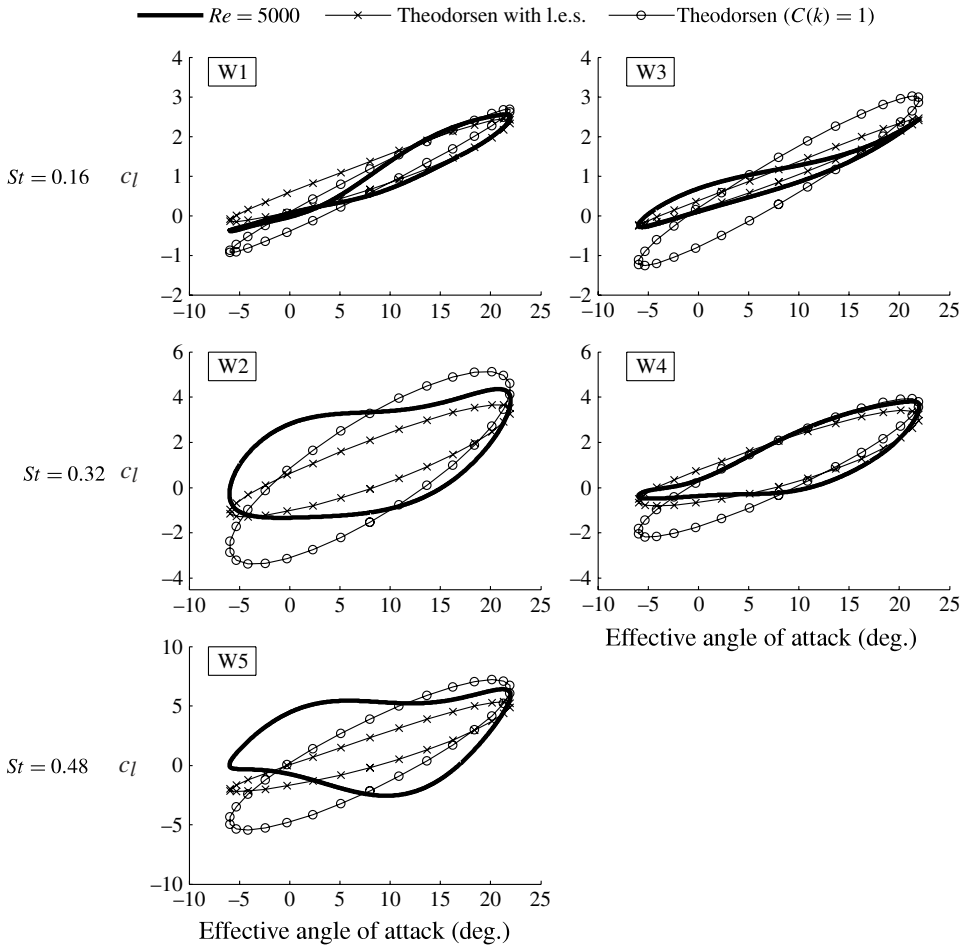
FIGURE 21. Measured lift coefficients compared with the Theodorsen model with the leading-edge suction (l.e.s.) term, and the Theodorsen model with $C(k) = 1$.

leading-edge suction is small during the upstroke motion. In effect, the leading-edge suction term significantly improved the agreement with the measured lift coefficient compared to the standard Theodorsen model shown in figure 19 for cases W1, W3 and W4. For cases W2 and W5, the Theodorsen model with $C(k) = 1$ still performed better than the Theodorsen model with the leading-edge suction term.

In summary, figures 19–21 suggest three main conclusions: (i) Garrick's formulation inaccurately accounts for the leading-edge suction as thrust rather than lift for aerofoil kinematics that produce LEV; (ii) ignoring the effect of the wake, or setting $C(k) = 1$, correctly accounts for the force coefficient profile from an increase in bound vorticity that results from the formation of LEV; and (iii) the leading-edge suction analogy proposed by Polhamus (1966) improves the accuracy of the theoretical model when LEV is present, but the $C(k) = 1$ assumption provides a better approximation to the experimental results for high-St and high-k kinematics. For cases W1, W3 and W4, it can be said that the amount of leading-edge suction added to the lift coefficient from the standard Theodorsen model is approximately equivalent to ignoring the effect
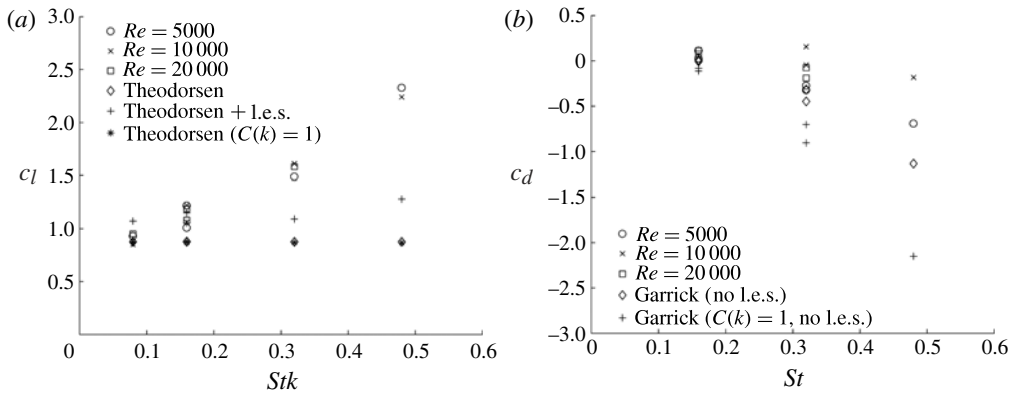
FIGURE 22. Measured and computed mean force coefficients. (*a*) Mean lift coefficient as a function of *Stk* gives the best correlation of measured data; (*b*) mean drag coefficient as a function of *St*.

of the shed wake during the downstroke motion. For W2 and W5, the leading-edge suction is insufficient to account for the rapid increase in the lift coefficient, perhaps due to a combination of high pitch rates and delayed formation of the LEV.

It is important to note that *St* is coupled to the pitch amplitude in the current study in order to maintain the same effective angle-of-attack profile for all *St*. Therefore, an increase in *St* also increases $|\theta_0|$, which effectively increases the value of the force coefficients computed from the models proposed by Theodorsen and Garrick. One of the main reasons for achieving high *St*, in the range 0.25–0.35, is to increase the pitch amplitude such that more normal force can be projected towards thrust during the downstroke motion, since the current study has found that the normal force component is the main source of unsteady force generation. As for lift, higher lift coefficients are recorded for higher-*St* kinematics.

The theoretical and measured mean force coefficients are presented in figure 22. The mean lift coefficients from the standard Theodorsen and from Theodorsen with $C(k) = 1$ remain similar at $c_l \approx 0.87$ for all cases. The addition of the leading-edge suction term from Garrick's formulation to the standard Theordorsen model significantly increases the mean lift coefficients. The mean drag coefficient using Garrick's formulation without the leading-edge suction term reports thrust for all cases except case W1, while setting $C(k) = 1$ significantly increases the mean thrust values for all cases. For the measured lift coefficient in figure 22(*a*), the mean values for all *Re* are in good agreement. The measured mean lift coefficient is significantly higher at high-*St* kinematics when compared with theoretical values. Figure 22(*b*) shows that Garrick's formulation over-predicts the mean thrust coefficient compared to measured values for all *Re*. The over-prediction arises during the upstroke motion where the shed LEV and TEV in the wake contribute to an increase in the pressure drag that is not accounted for properly in the model. In addition, Garrick's formulation also ignores the effect of viscosity, which will also result in over-prediction of the thrust.

The mean force coefficients show *St* dependence, where increase in *St* increases the mean values of both lift and thrust coefficients. For the same *St*, such as cases W1 and W3, a higher *k* value produces more lift. The mean lift coefficient for the standard Theodorsen and for Theodorsen with $C(k) = 1$ remains fixed at approximately 0.87 for all cases, while the standard Theodorsen model with the addition of the

leading-edge suction term provides better agreement with the measured lift coefficients. The measured lift coefficients for high-*St* and high-*k* cases are significantly higher than any models considered in the current study, and it appears to be that the delayed formation of the LEV and resulting convection of LEV in the chordwise direction during the upstroke motion produce lift rather than the downforce predicted by theory. The increase in lift during the upstroke motion increases the mean lift coefficient.

Overall, the agreement of force coefficients during the downstroke motion between the measured and theoretical models was improved by ignoring the effects of the wake. The leading-edge suction contributed to the lift more than to the drag for the cases presented here, supporting the analogy proposed by Polhamus (1966). A mismatch between measured results and theory was found during the upstroke motion due to shed LEV and TEV. A delay in the LEV formation allowed LEV to be attached to the aerofoil surface during the upstroke, which caused lift generation. When the LEV detached at the trailing edge, it caused an increase in pressure drag that is not taken into account by theoretical models.

4. Conclusions

This paper reports the unsteady flow development, LEV vortex dynamics and force generation in pitching and plunging flat-plate aerofoils at $Re = 5000$, 10 000 and 20 000 using PIV and direct force measurement. The Strouhal number range considered is between 0.10 and 0.48, which is relevant to flapping wing flight as well as to numerous biological flyers. The same sinusoidal effective angle-of-attack time history is used to isolate the effects of Strouhal number and reduced frequency in the flow dynamics and aerodynamic force generation. For the range of Strouhal numbers considered, the plunge motion required to achieve this constraint is not sinusoidal and the corresponding plunge motion history is derived in the paper. In order to enhance understanding of unsteady aerodynamics, linear potential flow models developed by Theodorsen (1935) and Garrick (1936) are compared to the experimental results. Despite the rather extensive simplifications, model results show reasonable agreement with the measurements. The present study successfully identifies limitations of the models and suggests modifications to improve agreement with experimental data. It is also shown that the *Re* effects are weak for the flat-plate aerofoils and kinematics considered.

Reduced frequency, *k*, is identified as the main parameter governing flow development. The normalized vorticity contours from PIV measurements showed slower LEV growth rate as the reduced frequency was increased, which subsequently delayed formation and shedding of TEV. However, the flow topology remained the same for all cases, regardless of chosen motion parameters.

The LEV circulation increased linearly as a function of the motion phase while the LEV size obeyed a power law. For kinematics with $k < 0.50$, peak circulation location was delayed as reduced frequency increased. For kinematics with $k > 0.50$, LEV circulation growth stopped at the end of the downstroke. In all cases, peak LEV circulation decreases with reduced frequency and increases slightly with Strouhal number. While the LEV growth rate depends on *k*, the LEV core trajectory with respect to the aerofoil was independent of motion parameters but was a function of effective angle of attack for $k \leqslant 1.0$ and $St \leqslant 0.20$. The only exception to this behaviour was for $k = 1$ and $St = 0.32$, where the LEV moved closer to the aerofoil and remained on the suction side of the aerofoil during the initial phases of the upstroke.

Both *St* and *k* parameters impact the measured force coefficient histories; however, the effect of *St* was more dominant than that of *k*. For the cases reported here, the collapse of the lift coefficient at high effective angle of attack observed in dynamic stall studies (McCroskey 1982; Rival & Tropea 2010) at reduced frequency $k < 0.2$ is not observed, which could be attributed to the LEV remaining relatively close to the aerofoil or non-circulatory effects becoming more important at higher reduced frequency. The entire force coefficient time histories were affected by *St*, where the peak values increased with increasing *St*. For the lift coefficient, the Theodorsen model with $C(k) = 1$ successfully captured the lift coefficient history at high effective angles of attack during the downstroke part of the motion, which suggests no vorticity shedding into the wake during this phase of the motion, as documented by PIV measurements. For the drag coefficient, inclusion of the leading-edge suction term, in addition to the normal force component, resulted in over-prediction of the thrust. A large discrepancy in the drag coefficient during the upstroke motion was noted due to shed LEV and TEV in the wake, which is not captured in Garrick's formulation. The leading-edge suction analogy proposed by Polhamus (1966), where the leading-edge suction term was directly added to the standard Theodorsen model, improves the agreement with the measurement results. However, the leading-edge suction term alone was insufficient to account for the large discrepancies in the lift for high-*St* and high-*k* kinematics.

In summary, we have studied the flow evolution and aerodynamic force generation of pitching and plunging aerofoils for the same effective angle-of-attack history. The amplitude of the effective angle-of-attack oscillation is large enough to cause the formation of an LEV during the downstroke. It is shown that the effect of Reynolds number is small. Two non-dimensional parameters control the evolution and flow dynamics: reduced frequency and Strouhal number. Reduced frequency, which is the ratio of convective time to motion period, is the more important parameter controlling the flow evolution. As the motion period decreases, the LEV development and detachment are delayed. Strouhal number has a relatively small effect in this process, affecting only LEV circulation by a small amount. Furthermore, it is found that, at high reduced frequency, motion kinematics determine the maximum circulation of the LEV. Strouhal number, which is proportional to the ratio of plunge motion speed to free stream velocity, is the more important parameter controlling aerodynamic force generation. For the present cases, reduced frequency plays only a small role in aerodynamic force generation associated with the delayed development of the LEV. It is found that unsteady linear potential flow theory is in reasonable agreement with the measured lift coefficients. During the downstroke, better agreement is found using the quasi-steady assumption $C(k) = 1$. Linear potential flow theory significantly over-predicts the thrust, and better agreement is found when the contribution of the leading-edge suction to the thrust is ignored.

REFERENCES

ANDERSON, J. M., STREITLEIN, K., BARRETT, D. S. & TRIANTAFYLLOU, M. S. 1998 Oscillating foils of high propulsive efficiency. *J. Fluid Mech.* **360**, 41–72.

BAIK, Y. 2011 Unsteady force generation and vortex dynamics of pitching and plunging aerofoils at low Reynolds number. PhD thesis, University of Michigan.

BAIK, Y., RAUSCH, J. M., BERNAL, L. P., SHYY, W. & OL, M. 2010 Experimental study of governing parameters in pitching and plunging aerofoil at low Reynolds number. *AIAA Paper* 2010-0388.

BIRCH, J. M., DICKSON, W. B. & DICKINSON, M. H. 2004 Force production and flow structure of the leading edge vortex on flapping wings. *J. Expl Biol.* **207**, 1063–1072.

BISPLINGHOFF, R. L., ASHLEY, H. & HALFMAN, R. L. 1996 *Aeroelasticity*. Dover.

CHAKRABORTY, P., BALACHANDAR, S. & ADRIAN, R. J. 2005 On the relationship between local vortex identification schemes. *J. Fluid Mech.* **535**, 189–214.

DABIRI, J. O. 2009 Optimal vortex formation as a unifying principle in biological propulsion. *Annu. Rev. Fluid Mech.* **41**, 17–33.

DICKINSON, M. H. & GOTZ, K. G. 1993 Unsteady aerodynamic performance on model wings at low Reynolds numbers. *J. Expl Biol.* **174**, 45–64.

VON ELLENRIEDER, K. D. & POSTHOS, S. 2008 PIV measurements of the asymmetric wake of a two-dimensional heaving hydrofoil. *Exp. Fluids* **44**, 733–745.

ELLINGTON, C. P., VAN DEN BERG, C., WILLMOTT, A. P. & THOMAS, A. L. R. 1996 Leading-edge vortices in insect flight. *Nature* **384**, 626–630.

GARRICK, I. E. 1936 Propulsion of a flapping and oscillating aerofoil. NASA Tech. Rep. 567.

GHARIB, M., RAMBOD, E. & SHARIFF, K. 1998 A universal time scale for vortex ring formation. *J. Fluid Mech.* **360**, 121–140.

GODOY-DIANA, R., AIDER, J. L. & WESFRIED, J. E. 2009 A model for the symmetry breaking of the reverse Bénard–von Kármán vortex street produced by a flapping foil. *J. Fluid Mech.* **622**, 23–32.

GRAFTIEAUX, L., MICHARD, M. & GROSJEAN, N. 2001 Combining PIV, POD and vortex identification algorithms for the study of unsteady turbulent swirling flows. *Meas. Sci. Tech.* **12**, 1422–1429.

GRANLUND, K., OL, M. & BERNAL, L. 2011 Experiments on pitching plates: force and flow field measurements at low Reynolds numbers. *AIAA Paper* 2011-0872.

HOVER, F. S., HAUGSDAL, O. & TRIANTAFYLLOU, M. S. 2004 Forces on oscillating foils for propulsion and maneuvering. *J. Fluid Struct.* **19**, 37–47.

JONES, A. R. & BABINSKY, H. 2010 Unsteady lift generation on rotating wings at low Reynolds numbers. *J. Aircraft* **47**, 1013–1021.

KANG, C.-K., BAIK, Y., BERNAL, L. P., OL, M. V. & SHYY, W. 2009 Fluid dynamics of pitching and plunging aerofoils of Reynolds number between 1×10^4 and 6×10^4. *AIAA Paper* 2009-536.

VON KÁRMÁN, T. & SEARS, W. R. 1938 Airfoil theory for non-uniform motion. *J. Aeronaut. Sci.* **5**, 379–390.

KOOCHESFAHANI, M. M. 1989 Vortical patterns in the wake of an oscillating aerofoil. *AIAA J.* **27**, 1200–1205.

KRUEGER, P., DABIRI, J. O. & GHARIB, M. 2006 The formation number of vortex rings formed in uniform background co-flow. *J. Fluid Mech.* **556**, 147–166.

LAI, J. C. S. & PLATZER, M. 1999 Jet characteristics of a plunging aerofoil. *AIAA J.* **37**, 1529–1537.

LIGHTHILL, M. J. 1969 Hydromechanics of aquatic animal propulsion. *Annu. Rev. Fluid Mech.* **1**, 413–446.

LUA, K. B., LIM, T. T., YEO, K. S. & OO, G. Y. 2007 Wake-structure formation of a heaving two-dimensional elliptic aerofoil. *AIAA J.* **45**, 1571–1583.

MAXWORTHY, T. 1981 The fluid dynamics of insect flight. *Annu. Rev. Fluid Mech.* **13**, 329–350.

MCCROSKEY, W. J. 1981 The phenomenon of dynamic stall. *Tech. Rep.* 81264. NASA Tech. Mem.

MCCROSKEY, W. J. 1982 Unsteady aerofoils. *Annu. Rev. Fluid Mech* **14**, 285–311.

MCGOWAN, G. Z., GRANLUND, K., OL, M. V., GOPALARATHNAM, A. & EDWARDS, J. R. 2011 Investigations of lift-based pitch–plunge equivalence for aerofoils at low Reynolds numbers. *AIAA J.* **49**, 1511–1524.

MILANO, M. & GHARIB, M. 2005 Uncovering the physics of flapping flat plates with artificial evolution. *J. Fluid Mech.* **534**, 403–409.

OHMI, K., COUTANCEAU, M., DAUBE, O. & LOC, T. P. 1991 Further experiments on vortex formation around an oscillating and translating aerofoil at large incidences. *J. Fluid Mech.* **225**, 607–630.

OHMI, K., COUTANCEAU, M., LOC, T. P. & DULIEU, A. 1990 Vortex formation around an oscillating and translating aerofoil at large incidences. *J. Fluid Mech.* **211**, 37–60.

OL, M., BERNAL, L. P., KANG, C. & SHYY, W. 2009 Shallow and deep dynamic stall for flapping low Reynolds number aerofoils. *Exp. Fluids* **46**, 883–901.

OL, M., MCAULIFFE, B. R., HANFF, E. S., SCHOLZ, U. & KAEHLER, CH. 2005 Comparison of laminar separation bubble measurements on a low Reynolds number aerofoil in three facilities. *AIAA Paper* 2005-5149.

PLATZER, M., JONES, K., YOUNG, J. & LAI, J. 2008 Flapping wing aerodynamics: progress and challenges. *AIAA J.* **46**, 2136–2149.

POLHAMUS, E. C. 1966 A concept of the vortex lift of sharp-edge delta wings based on a leading-edge-suction analogy. *Tech. Rep.* NASA Technical Note.

READ, D. A., HOVER, F. S. & TRIANTAFYLLOU, M. S. 2003 Effect of angle of attack profiles in flapping foil propulsion. *J. Fluid Struct.* **17**, 163–183.

RINGUETTE, M., MICHELLE, M. & GHARIB, M. 2007 Role of the tip vortex in the force generation of low-aspect-ratio normal flat plates. *J. Fluid Mech.* **581**, 453–468.

RIVAL, D., PRANGEMEIER, T. & TROPEA, C. 2009 The influence of aerofoil kinematics on the formation of leading-edge vortices in bio-inspired flight. *Exp. Fluids* **46**, 823–833.

RIVAL, D. & TROPEA, C. 2010 Characteristics of pitching and plunging aerofoils under dynamic-stall conditions. *J. Aircraft* **47**, 80–86.

SANE, S. P. 2003 The aerodynamics of insect flight. *J. Expl Biol.* **206**, 4195–4208.

SHYY, W., LIAN, Y., VIIERU, D. & LIU, H. 2008 *Aerodynamics of Low Reynolds Number Flyers*. Cambridge University Press.

SHYY, W. & LIU, H. 2007 Flapping wings and aerodynamics lift: the role of leading-edge vortices. *AIAA J.* **45**, 2817–2819.

STRICKLAND, J. H. & GRAHAM, G. M. 1987 Force coefficients for a NACA-0015 aerofoil undergoing constant pitch rate motions. *AIAA J.* **25**, 622–624.

TAYLOR, G. K., NUDDS, R. L. & THOMAS, A. L. R. 2004 Flying and swimming animals cruise at a Strouhal number tuned for high power efficiency. *J. Fluid Struct.* **19**, 37–47.

THEODORSEN, T. 1935 General theory of aerodynamic instability and the mechanism of flutter. NACA Tech. Rep. 496.

TRIANTAFYLLOU, G. S., TRIANTAFYLLOU, M. S. & GROSENBAUGH, M. A. 1992 Optimal thrust development in oscillating foils with applications to fish propulsion. *J. Fluid Struct.* **7**, 205–224.

VISBAL, M. R. & SHANG, J. S. 1989 Investigation of the flow structure around a rapidly pitching aerofoil. *AIAA J.* **27**, 1044–1051.

YOUNG, J. & LAI, J. C. S. 2004 Oscillation frequency and amplitude effects on the wake of a punging aerofoil. *AIAA J.* **42**, 2042–2052.